

Core-collapse, superluminous, and gamma-ray burst supernova host galaxy populations at low redshift: the importance of dwarf and starbursting galaxies

K. Taggart,¹[★] D. A. Perley¹

¹ Astrophysics Research Institute, Liverpool John Moores University, 146 Brownlow Hill, Liverpool L3 5RF

Accepted XXX. Received YYY; in original form ZZZ

ABSTRACT

We present a comprehensive study of an unbiased sample of 84 nearby ($\langle z \rangle = 0.016$) core-collapse supernova (CCSN) host galaxies drawn from the All-Sky Automated Survey for Supernovae (ASAS-SN) for direct comparison to the nearest LGRB and SLSN hosts. We use public imaging surveys to gather multi-wavelength photometry for all CCSN host galaxies and fit their spectral energy distributions (SEDs) to derive stellar masses and integrated star formation rates. CCSNe populate galaxies across a wide range of stellar masses, from blue and compact dwarf galaxies to large spiral galaxies. We find 40^{+6}_{-5} per cent of CCSNe are in dwarf galaxies ($M_* < 10^9 M_\odot$) and 2^{+3}_{-1} per cent are in dwarf starburst galaxies ($sSFR > 10^{-8} \text{ yr}^{-1}$). We reanalyse low-redshift SLSN and LGRB hosts from the literature (out to $z < 0.3$) in a homogeneous way and compare against the CCSN host sample. We find that the relative SLSN to CCSN supernova rate is increased in low-mass galaxies and at high specific star-formation rates. These parameters are strongly covariant and we cannot break the degeneracy between them with our current sample. Larger unbiased samples of CCSNe from projects such as ZTF and LSST will be needed to determine whether host-galaxy mass (a proxy for metallicity) or specific star-formation rate (a proxy for star-formation intensity and potential IMF variation) is more fundamental in driving the preference for SLSNe and LGRBs in unusual galaxy environments.

Key words: transients: supernovae – transients: gamma-ray bursts – galaxies: dwarf – galaxies: photometry – galaxies: star formation

1 INTRODUCTION

Massive stars ($> 8 M_\odot$) evolve rapidly, and after a short life (up to a few tens of million years), they die in violent core-collapse supernova (CCSN) explosions. CCSNe have a profound influence on their environment: they produce heavy elements and deposit large amounts of energy into their environments, driving feedback and chemical evolution in galaxies (e.g., Chevalier 1977). In addition, because of the short progenitor lifetime, the volumetric CCSN rate is a direct tracer of star-formation. Thus, CCSNe can be used to quantify the contribution to cosmic star-formation from distinct galaxy subclasses and to pinpoint rare individual star-forming galaxies, especially at low stellar mass, where galaxy catalogues are incomplete (e.g., Sedgwick et al. 2019).

Candidate CCSN progenitors are diverse, as are the explosion properties they produce. Observations of CCSN explosions and their progenitors provide a means to test theories of stellar evolution and the explosion channels of very massive stars. However,

despite the importance of CCSNe to many areas of astrophysics, mapping a star’s evolution from its beginning to end, fully accounting for complicating factors such as metallicity, binarity, and rotation remains an open problem.

Observationally, CCSNe are classified into types I and II based on the presence (II) or absence (I) of hydrogen emission lines in their spectra at maximum light (Filippenko 1997). Some CCSN progenitors lose part/all of their hydrogen stellar envelope prior to their explosion due to stellar winds (Maeder & Meynet 2000) or binary mass transfer (Podsiadlowski et al. 1992) and are observed as a helium-rich (Ib and IIf) or helium-poor (Ic) stripped-envelope SN (SE-SN; Smartt 2009). In recent years, due to a new generation of all-sky surveys and ever-increasing observational capabilities, many new types of stellar explosion have emerged beyond this classical picture. One example is superluminous supernovae (SLSNe) which are likewise classified into types I and II, but whose extreme luminosities exceed ordinary CCSNe by a factor of 10–100 (Quimby et al. 2011; Gal-Yam 2012) and likely require an additional power source.

SLSN-II are most likely powered by SN interaction with a

* E-mail: K.L.Taggart@2016.ljmu.ac.uk

dense circumstellar shell of hydrogen created by an ultra-massive star progenitor star before the explosion (Chevalier & Irwin 2011; Ginzburg & Balberg 2012; Moriya et al. 2013) or episodic mass-loss in a pulsational pair-instability explosion (PPISNe; Woosley et al. 2007; Chatzopoulos & Wheeler 2012). However, the mechanism that powers SLSN-I is still puzzling. In theory, an extremely massive stellar core (Moriya et al. 2010; Young et al. 2010) could produce enough ^{56}Ni to power a SLSN via radioactive decay, but mass-loss during a star’s lifetime makes it difficult to retain such a massive core. Several other theoretical mechanisms have been proposed to explain SLSN-I, including interaction with non-hydrogen circumstellar-material (Chatzopoulos & Wheeler 2012; Sorokina et al. 2016; Vreeswijk et al. 2017), a Pair-Instability SN (PISN, Barkat et al. 1967; Rakavy & Shaviv 1967) from a very massive *and* metal-poor star ($\sim 0.2 \text{ Z}_\odot$; Yusof et al. 2013) or an engine-driven scenario (similar to that invoked for long-duration gamma-ray bursts) which would provide a long-lived energy source behind the SN ejecta (e.g., Kasen & Bildsten 2010; Metzger et al. 2015).

Long-duration gamma-ray bursts (LGRBs) are brief, but extremely luminous flashes of high-energy radiation associated with the formation of a relativistic jet from a ‘central engine’ (a fast-spinning neutron star or black hole) at the centre of a collapsing and rapidly rotating massive stellar core. While most LGRBs occur at very high redshifts, events that occur sufficiently nearby are typically observed in association with CCSNe (Galama et al. 1998; Hjorth et al. 2003; Woosley & Bloom 2006); these SNe are universally luminous, helium-poor SE-SN with very broad spectral features (Ic-BL) indicating large ejecta velocities (Cano et al. 2017b). Despite this tight association, it is not yet firmly established whether all LGRBs occur in association with SN Ic-BL, and vice versa. Two LGRBs from 2006 have no reported SN association to deep limits (Fynbo et al. 2006; Gal-Yam et al. 2006; Gehrels et al. 2006; Della Valle et al. 2006), and SN Ic-BL are frequently found blindly in optical surveys without any association with a LGRB. A small number of Ic-BL have shown a bright radio counterpart suggesting the presence of energetic, relativistic ejecta from a central-engine similar to what is seen in GRBs (Soderberg et al. 2010; Corsi et al. 2016), but most of them do not show this signature. The nature of the progenitor is also uncertain, including whether the progenitor is a single star (Yoon et al. 2006) or a binary system (Cantiello et al. 2007).

The physical powering mechanisms and progenitors of SLSNe and LGRBs are still under debate and their low volumetric rate (Quimby et al. 2013; Prajs et al. 2017) suggests that it is highly unlikely that pre-explosion imaging will ever uncover the progenitor properties through direct detection of the progenitor star. Thus, another way to constrain progenitor models for SLSNe and LGRBs is to analyse the properties of the galaxies they inhabit, which can be tied to the SN progenitor models themselves. For example, a PISN likely requires a low-metallicity, star-forming environment to produce a star with sufficient initial mass (and to avoid losing its mass in line-driven winds). And single-star progenitor mechanisms for central-engine models of LGRBs also likely require a low metallicity, since line-driven winds would otherwise quickly sap the progenitor of its rotational energy. More exotically, some models postulate that LGRBs and/or SLSNe may arise as the result of runaway collisions in young and dense star clusters (van den Heuvel & Portegies Zwart 2013): in this scenario, one may expect to find SLSN more frequently in galaxies undergoing an exceptionally high rate of star formation, even after accounting for the fact that any CCSN is proportionally more likely to occur in a galaxy with a high SFR.

There is ample evidence that LGRB and SLSN-I host galaxies differ from the bulk of the star-forming galaxy population. Specifically, both LGRBs and SLSNe-I occur preferentially in faint, low-mass galaxies with irregular structure (Neill et al. 2011; Lunnan et al. 2014; Angus et al. 2016; Fruchter et al. 2006). Whereas CCSNe are found in massive spiral galaxies: low-z CCSN samples (prior to untargeted all-sky surveys) were found via targeted surveys of nearby galaxies therefore always found in massive, nearby galaxies and half of high-z CCSN (found blindly in deep surveys covering small fields of view) explode in spiral galaxies (Svensson et al. 2010).

There is also good evidence in particular that metallicity affects SLSN and LGRB production: high-metallicity environments rarely produce LGRBs (Krühler et al. 2015; Perley et al. 2016b) or SLSNe (Perley et al. 2016a; Schulze et al. 2018; Chen et al. 2017a)¹. In addition, SE-SNe and non-stripped SNe also appear to have differences in their environments. Graur et al. (2017a,b) found that the relative rate of Ib/c SE-SNe vs. non-stripped CCSNe declines in low-mass ($<10^{10} \text{ M}_\odot$) galaxies; they are underrepresented by a factor of ~ 3 , which may favour a binary formation channel for SE-SNe. Nevertheless, there is some disagreement in the literature; Arcavi et al. (2010) found that while the relative rate of Ic SNe vs. non-stripped CCSNe decreased in low-mass galaxies, the relative rates of all other SE-SNe (Ic-BL, Ib, IIb) vs. non-stripped CCSNe increased in low-mass, low-metallicity galaxies, which may be a result of a reduced metallicity-driven mass loss causing some massive stars that would have exploded as a Ic SN in a metal-rich galaxy to retain some H and He and explode as a Ib/IIb event instead. There are also differences in the environments of SE-CCSN themselves. Ordinary Ic CCSNe are found in more metal-rich galaxies with lower sSFRs than their more energetic Ic-BL cousins (with and without LGRB associations) which may suggest that Ic-BL harbour LGRB jets from a compact central engine, which in turn requires a low-metallicity environment, whereas ordinary Ic SNe may not require such an environment (Modjaz et al. 2019).

Additionally, there are also some indications that metallicity alone may not fully explain the unusual properties of the host galaxies of SLSNe and LGRBs. In particular, many SLSN-I hosts show very high specific star-formation rates (sSFR=SFR/M_{*}) as well as low metallicities, evidenced by their very high equivalent widths (Leloudas et al. 2015): as many as ~ 50 per cent of SLSNe-I are found in extreme emission line galaxies (EELGs; Leloudas et al. 2015), defined by a very large equivalent widths in nebular lines associated with active star-formation. While sometimes attributed to a very young progenitor that simply explodes earlier than other types of SNe (Leloudas et al. 2015; Thöne et al. 2015), it could also point towards an *intrinsic* preference in starbursting galaxies that favours the production of SLSNe, such as a top-heavy IMF (e.g., Dabringhausen et al. 2009) or the collisional model of van den Heuvel & Portegies Zwart (2013).

A complicating factor is that all key galaxy observational parameters we may want to use to diagnose the nature of the progenitor (e.g., stellar mass, metallicity and sSFR) correlate across the star-forming galaxy population (e.g., Tremonti et al. 2004; Salim

¹ However, this is not the entire picture since over the past few years, as the statistical sizes of nearby SLSN and LGRBs have increased, there have been a handful of cases of large spiral galaxies with high-metallicities hosting SLSN-I (MLS121104, PTF10uhf, SN 2017egm, Lunnan et al. 2014; Perley et al. 2016c; Dong et al. 2017) and nearby LGRBs (e.g., Izzo et al. 2019).

et al. 2007). For example, a low-mass and low-metallicity galaxy tends to have a star-formation history with short bursts of concentrated star-formation and therefore is more likely to be observed as a starburst than a high-mass and high-metallicity galaxy. Thus, it is still unclear to what extent the environmental properties of SLSNe and LGRBs (low-mass, low metallicity and high sSFR) reflect their specific physical influences (progenitor and explosions mechanism).

In order to disentangle the role of metallicity and SFR and to determine if both properties are equally important in governing SLSN and LGRB production, we need an unbiased and representative sample of star-forming galaxies to provide testable predictions for where we might expect SLSNe and LGRBs to occur under various hypothesis about their formation preferences. Ideally, the sample of star-forming galaxies should be selected in the same manner as a SLSN or a LGRB—via the explosion of a massive star as detected in a time-domain imaging survey—to minimise the large methodological differences between selecting via SNe vs. selecting via galaxy counts in flux-limited surveys. In other words, we require a high-quality sample of ‘ordinary’ CCSNe.

This sample must have several properties. First, it must enclose a sufficiently large volume such that it is not subject to strong cosmic variance effects. Second, the SNe must be discovered in an unbiased way (not via galaxy-targeted surveys). Third, the sample must be able to securely distinguish CCSNe from Ia SNe for all transients, ideally via spectroscopy. Finally, it must have multi-wavelength galaxy data from UV to NIR in order to derive physical parameters for the hosts. Few existing SN samples have these properties, and until recently none of them were at low redshifts where detailed host studies are most practical. Examples of other large, untargeted SN samples include SDSS (Frieman et al. 2008; Sako et al. 2008) and SNLS (Bazin et al. 2009) but these surveys are not spectroscopically complete and this leads to ambiguities in the classifications.

In this paper we address this need by compiling a large, unbiased, representative sample of CCSN host galaxies (which we assume sample the explosions of ‘typical’ massive stars, unlike SLSNe and LGRBs). We provide photometry of this sample with integrated UV-through-NIR SEDs and stellar masses and star-formation rates derived from these measurements. We investigate star-formation within the CCSN host galaxy sample and compare to a sample of SLSN and LGRBs.

The paper is organised as follows: Section 2 describes how the transient host galaxies are selected to form our CCSN, SLSN and LGRB samples. In Section 3, we describe our photometry method and show all other archival photometry which has been used in this paper. In Section 4, we present the methodology used to measure the star-formation rates and stellar masses of each host galaxy based on UV through NIR colours. In Section 5 we show our results and in Section 6, we summarise our findings and present our conclusions. Throughout this paper we adopt Λ CDM cosmology, with $\Omega_0 = 0.27$, $\Omega_\Lambda = 0.73$ and $H_0 = 70\text{km}\text{s}^{-1}\text{Mpc}^{-1}$ (Komatsu et al. 2011).

2 HOST GALAXY SAMPLES

2.1 Core collapse supernovae

A variety of galaxy-untargeted SN catalogues exist, including the Dark Energy Survey (Flaugher 2005), Catalina Real-Time Survey (Drake et al. 2009), the Palomar Transient Factory (Law

et al. 2009), SuperNova Legacy Survey (Bazin et al. 2009), Pan-STARRS (Kaiser et al. 2002), La Silla Quest (Hadjyska et al. 2012), the Gaia transient survey (Hodgkin et al. 2013), SkyMapper (Keller et al. 2007), SDSS Supernova Survey (Frieman et al. 2008) and the All-Sky Automated Survey for Supernovae (ASAS-SN; Shappee et al. 2014). We draw our CCSN sample from ASAS-SN for two reasons. First, it is shallow ($m_{V,\text{limit}} \sim 17$ mag) but is all-sky, so the SNe it finds are generally very nearby, where excellent photometric galaxy information exists in public catalogues. The ASAS-SN sample is spectroscopically complete for SNe with peak V -band light curve magnitudes $m_V < 15.8$ and is roughly 50 per cent complete at $m_V \sim 17$ (Holien et al. 2017a). Second, almost all SNe discovered by ASAS-SN are bright enough (even with small telescopes) for the global SN community to follow-up, spectroscopically classify and derive a redshift estimate. This is important since we need an unambiguous sample of CCSN selected host galaxies and we require a reliable SN redshift estimate for our host analysis.

We compile all spectroscopically confirmed CCSN discovered by ASAS-SN (2013–2014, 2015, 2016, 2017; Holien et al. 2017a,b,c, 2019), adopting any SN classifications and redshift estimates which were updated since the initial classification was made. There are two exceptions, both of which were claimed to be SLSN: ASAS-SN 15lh was classified as a SLSN-I (Dong et al. 2016), but was omitted from the CCSN sample since it is not well understood whether this event is a SLSN or a tidal disruption event (Leloudas et al. 2016; Margutti et al. 2017) and ASAS-SN 17jz was re-classified as a SLSN-II, but its classification is ambiguous; it could be a very luminous SN-II (Xhakaj et al. 2017) or alternatively it could be an AGN (Arcavi et al. 2017). In any case, these events are not ‘typical’ CCSNe and we exclude them from the CCSN sample. We limit our sample to a declination greater than -30° because uniform, public, deep optical survey data is not available across the entire southern hemisphere. We also impose a galactic latitude cut ($|b| > 15^\circ$) in order to eliminate those galaxies where stellar crowding significantly affects the photometry of the galaxies and thus remove ASAS-SN 17ny and 17kr from the sample.

Our sample thus defined is comprised of 84 SNe discovered from 2013 to the end of 2017. The redshift distribution covers the range 0.0024 – 0.08, with a median value of 0.016. A table with details of these galaxies can be found in Appendix B1–B. A mosaic showing our ASAS-SN CCSN host galaxy sample is provided in Fig. 1. We use methods detailed by Lupton et al. (2004) to convert PS1 *gri* images into a colour composite image. Each cutout has a constant physical size scale in the rest frame of the SN host of 21 kpc on each side and a scale bar showing an angular size of 10 arcsec is shown on each cutout.

2.2 Superluminous supernovae

We collate our initial SLSN sample based on archival SLSN in the literature. We include SLSN hosts from Neill et al. (2011)², SUSHIES (Schulze et al. 2018) and PTF (Perley et al. 2016c). In addition, we include five candidates identified by Quimby et al. (2018) following their reanalysis of archival PTF spectra: two likely SLSN-I (PTF 12gty and PTF12hni) and three possible SLSNe-I

² We do not include SN1995av and SN1997cy since their classifications are unclear, SN1997cy could be a SN Ia or IIn and may be associated with a LGRB

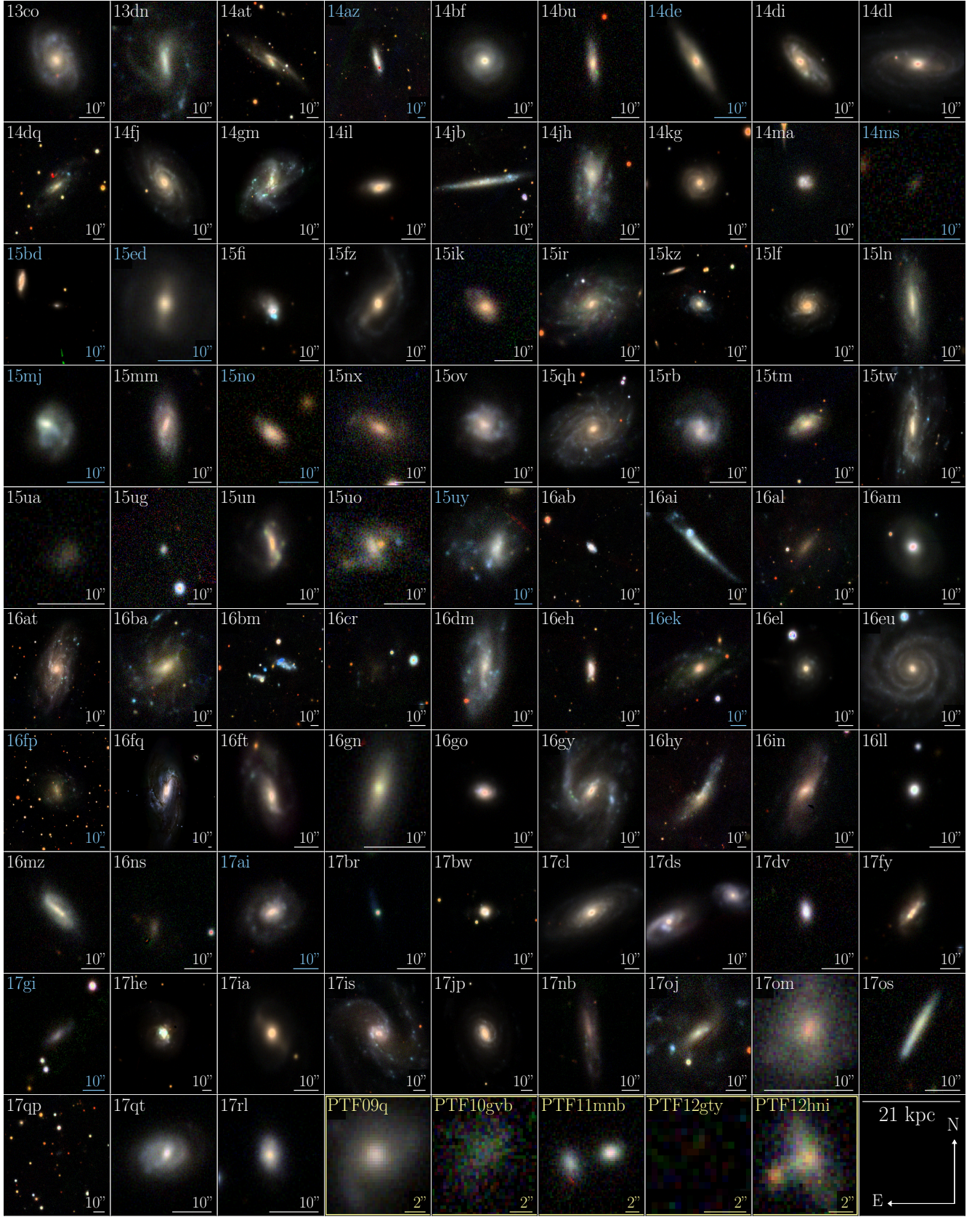


Figure 1. Mosaic showing RGB (*gri* PS1) colour composite images of our ASAS-SN CCSN host galaxy sample. Images labelled in white text are Type II CCSNe (excluding IIb) and images in blue are stripped-envelope SNe of type Ib/c or IIb. Each image has a constant physical size scale of 21 kpc in diameter at the redshift of the host galaxy and an angular scale of 10 arcsec is shown on each individual cutout. The image of low surface-brightness SN host 16ns is after the subtraction of a bright ($m \sim 17$) foreground star. The 5 PTF SLSN candidates that were discovered in the archival data are also included in last row of the figure in yellow text. The same physical size as the CCSN is used, but with a scale bar of 2 arcsec due to their higher redshift nature.

Table 1. Division of transient types within our samples.

Transient Type	Number
CCSN-IIb	4
CCSN-Ib/Ic	9
CCSN-II	71
CCSN Total	84
SLSN-I	29
Possible SLSN-I	3
SLSN-II	21
SLSN Total	53
LGRB-SN	12
SN-less LGRB	5
LGRB Total	17

Table 2. New PTF SLSN-I candidates from archival PTF search.

PTF ID	M_{peak}	$\alpha(2000)$	$\delta(2000)$	z	$E(B-V)$
09q*	~−20	12:24:50.11	+08:25:58.8	0.09	0.021
10gzb*	−19.6 [1]	12:15:32.28	+40:18:09.5	0.098	0.022
11mnb*	−18.9 [1]	00:34:13.25	+02:48:31.4	0.0603	0.016
12gty	−20.1 [2]	16:01:15.23	+21:23:17.4	0.1768	0.061
12hni	−19.9 [2]	22:31:55.86	−06:47:49.0	0.1056	0.054

Notes. Possible SLSN-I from [Quimby et al. \(2018\)](#) are indicated by a *; host analysis is done, but not included the SLSN statistical analysis due to uncertainty about the nature of the classification. 09q is reclassified as a SN Ia in [Modjaz et al. 2019](#).

References: [1] [Quimby et al. \(2018\)](#), [2] [De Cia et al. \(2018\)](#).

(PTF09q, PTF10gzb and PTF11mnb) at slightly lower luminosities ($M > -21$ mag) than the PTF sample of SLSN host galaxies by [Perley et al. \(2016c\)](#). These SN properties are summarised in Table 2. Rest frame g -band magnitudes for PTF12gty and PTF12hni are taken from [De Cia et al. \(2018\)](#) and PTF09q, PTF10gzb and PTF11mnb from [Quimby et al. \(2018\)](#). Thumbnail images of each host are shown in the bottom row of Fig. 1; the physical scale is the same as for the CCSN hosts, with a yellow scale bar of 2 arcsec.

We restrict our analysis to SLSNe with a redshift of $z < 0.3$ for two main reasons. First, more distant SLSNe are likely to be an incomplete sample due to the increased difficulty in spectroscopically confirming members of this class without a bright associated host galaxy. Second, we wish to reduce cosmic evolution effects when comparing to our $z \sim 0.02$ CCSN sample. After making this cut and excluding PTF09q, PTF10gzb and PTF11mnb, our final statistical sample consists of 29 SLSN-I and 21 SLSN-II in total.

2.3 LGRBs

Our LGRB sample consists of all $z < 0.3$ LGRBs discovered prior to the end of 2017 with an associated optical counterpart: a supernova, an optical afterglow, or both. The requirement for an optical afterglow is imposed to better match the optical selection of SNe used for comparison and to ensure a high degree of confidence in the host-galaxy association: while many additional low- z LGRBs have reported based on X-ray associations alone, it is difficult to rule out the possibility that these are higher- z events seen in coincidence with a foreground galaxy. This sample is comprised of 17 LGRBs; 12 which have confirmed SN associations and 5 without any reported SN (see Table 3).

Of the 5 LGRBs without SNe, two are highly-publicised events from 2006 for which a SN was ruled out to deep limits, LGRBs 060505 and 060614 ([Fynbo et al. 2006](#); [Gal-Yam et al.](#)

Table 3. Table of LGRB sources with and without SN associations. SN names and discovery reports are referenced and photometric (P) or spectroscopic (S) reports are indicated.

LGRB	SN name	SN Reference
980425	1998bw	[1,S]
020903	SN [†]	[1,S]
030329A	2003dh	[1,S]
031203	2003lw	[1,S]
050826	–	–
060218	2006aj	[1,S]
060505	–	–
060614	–	–
080517	–	–
100316D	2010bh	[1,S]
111225A	–	–
120422A	2012bz	[1,S]
130702A	2013dx	[1,S]
150518A	SN [†]	[1,P]
150818A	SN [†]	[1,S]
161219B	2016jca	[2–6,S]
171205	2017iuk	[7–13,S]

Notes. [†]In these cases, the LGRBs do have associated SN but there is no known SN name designation on TNS.

References: [1] Refer to Table 4. in [Cano et al. \(2017b\)](#), [2] [de Ugarte Postigo et al. \(2016\)](#), [3] [Volnova et al. \(2017\)](#), [4] [Chen et al. \(2017b\)](#), [5] [Ashall et al. \(2019\)](#), [6] [Cano et al. \(2017a\)](#), [7] [de Ugarte Postigo et al. \(2017\)](#), [8] [Cobb \(2017\)](#), [9] [Prentice et al. \(2017\)](#), [10] [D'Elia et al. \(2018\)](#), [11] [Wang et al. \(2018\)](#), [12] [Suzuki et al. \(2019\)](#), [13] [Izzo et al. \(2019\)](#).

2006; [Della Valle et al. 2006](#); [Gehrels et al. 2006](#)). These appear to have genuinely different progenitors and/or explosion mechanisms from ordinary SN-associated long-duration GRBs, a possibility that makes scrutiny of their host properties particularly relevant. The remaining events, LGRBs 050826, 080517 and 111225A, have relatively poor constraints on the extinction column towards the LGRB and/or on the presence of a SN peaking 1–3 weeks after the event (e.g., [Stanway et al. 2015](#)).

3 PHOTOMETRY

3.1 CCSN host multi-wavelength data

The galaxies in our CCSN sample are nearby ($z < 0.08$), so most are detectable in all-sky multi-wavelength surveys. Thus our primary image and source catalogues were public surveys. We use images from: the *Galaxy Evolution Explorer* (*GALEX*; [Martin et al. 2005](#)), the Panoramic Survey Telescope and Rapid Response System (PS1; [Kaiser et al. 2010](#)), the Sloan Digital sky survey (SDSS; [York et al. 2000](#)) and the Two Micron All-Sky Survey (2MASS; [Huchra et al. 2012](#)).

Our aim is to derive consistent mass and star-formation estimates for our host galaxy sample, thus we match aperture sizes across the optical and NIR wavelengths. This is particularly important for nearby and massive galaxies, since the aperture size can significantly increase or decrease the flux measurements. In addition, the automated pipeline of *GALEX*, 2MASS and *WISE* often incorrectly deblends galaxies with a large angular diameter on the sky and does not capture the low surface brightness parts of the galaxy.

If available, we use SDSS *ugriz* and *GALEX* FUV and NUV photometry from the NASA Sloan Atlas (NSA) (NSA; [Blanton et al. 2011](#)). The NSA is a unified catalogue of galaxies out to $z \sim$

0.05, optimised for nearby extended objects since the flux measurements are derived from reprocessed SDSS images with a better background subtraction (Blanton et al. 2011). We use the elliptical petrosian aperture photometry, with an elliptical aperture radius defined by the shape of the light profile of the galaxy as in Blanton et al. (2011) and Yasuda et al. (2001). The NSA flux measurements are available for about half of the northern hemisphere sample. Otherwise, we perform the photometry ourselves using optical images downloaded from Pan-STARRS DR1 (PS1) (Chambers et al. 2016; Magnier et al. 2016) and if SDSS u -band is available, we also perform that photometry.

We use the 2MASS extended source catalogue to obtain NIR brightness measurements in the J , H and K_s filters (Huchra et al. 2012). If the galaxy is in the NSA, we redo the 2MASS photometry with the same axis ratio and aperture orientation and use the curve of growth technique to adjust the size of the aperture. If the galaxy is not within the NSA, we check whether the 2MASS extended aperture (which fits an ellipse to the 20 mag arcsec^{-2} isophote in the K_s band and uses a curve of growth technique to capture low surface brightness flux of the galaxy) is adequate. In the cases of galaxies with small angular size, the aperture is usually adequate, but in the case of high mass, extended galaxies the aperture often misses a substantial fraction of the flux, thus we redo the 2MASS photometry.

3.2 Procedure for CCSN hosts

We perform aperture photometry using the python program PHOTUTILS³. We use an elliptical aperture and a curve-of-growth technique. We place the elliptical aperture at gradually increasing radii, measuring the flux in each aperture until the curve-of-growth levels, to the order of a few per cent, meaning the aperture is sufficiently large enough to include all of the host galaxy flux. We derive the uncertainties on these photometric measurements by using the galaxy aperture to determine the brightness of the background sky. We place the galaxy aperture 30 times within the image on 'blank' patches of the sky, making sure there is no overlap between apertures. We take the standard deviation of the measurements. In some cases, the galaxy is sufficiently massive and nearby that it covers a large angular diameter on the sky: placing 30 apertures of this size on blank patches of the sky is not feasible in these instances (the aperture region will always contain field sources), and in many cases the image itself is simply not large enough to place the aperture in 30 non-overlapping locations. In these cases, instead we remove the sources from the image and calculate the standard deviation of the sky background.

For image calibration we have used catalogues of stars (PS1 Object Catalogue, 2MASS Point Source Catalogue and the SDSS Imaging Catalogue) to calculate a zero point for each image. Instrumental magnitudes were calibrated directly to the AB system with photometry from PS1. All magnitudes were converted into the AB system (Oke & Gunn 1983). In addition, we correct all photometry for Galactic foreground extinction (Schlafly & Finkbeiner 2011).⁴

³ <https://github.com/astropy/photutils/tree/v0.3>

⁴ SN 2003ma pierces through the Large Magellanic Cloud, and the Galactic extinction of $E(B-V) = 0.348$ mag is a lower limit of what we would expect in this direction (Rest et al. 2011).

3.3 Galaxies requiring special attention

Some host galaxies in our sample required extra care when performing photometry and when fitting SED models. These galaxies are either diffuse, low surface brightness galaxies, galaxies which show signs of interaction with nearby galaxies or where there are foreground stars (or other objects) in front of the galaxy, or galaxies where there is some prior indication of AGN. Below we briefly describe each case where galaxies are treated individually.

3.3.1 Interacting galaxies

A significant number of host galaxies (in both the CCSN and extreme-SN samples) show evidence of physical companions, some of which appear to be in the process of interacting or merging. Our general philosophy is to mimic the photometry steps and subtraction we would do if these ASAS-SN galaxies were observed at $z \sim 0.2$ (for comparison to the LGRB and SLSN samples). We treat the merger as one system if it would not be resolved at $z \sim 0.2$ and is in the advanced merger stages, whereas if the galaxy could be resolved at those redshifts, then we measure the photometry of the single galaxy at the SN site.

ASAS-SN 14de: This galaxy is possibly undergoing an interaction or merger. This system would barely be detectable as 2 individual galaxies if it was discovered at a similar redshift to the SLSN/LGRB sample ($z \sim 0.2$), therefore we quote two different measurements for photometry: one of the entire system and one of the single galaxy from which the SN originated.

ASAS-SN 16bm: This galaxy is possibly undergoing an interaction or merger since the SN redshift $z = 0.007$ is at the same redshift of the other galaxy at $z = 0.00686$. The galaxies are 35 arcsec apart. However if the system was at $z \sim 0.2$ their centres would be separated only by 1 arcsecond. Thus, this system would barely be detectable as 2 individual galaxies if it was discovered at a similar redshift to the SLSN/LGRB sample ($z \sim 0.2$), therefore we quote two different measurements for photometry: one of the entire system and one of the single galaxy from which the SN originated. We use the photometry of the system for the SED fit.

ASAS-SN 17ds The host galaxy appears to have a companion in the PS1 imaging. However, an SDSS spectrum confirms that the redshift of this galaxy is $z = 0.046$, compared with the host galaxy with a redshift $z = 0.022$.

PTF12hni: There is a small, red object to east of the host galaxy (see panel 5 in Fig. 1.). A spectrum has been taken on 2017 July 13 with DEIMOS, on Keck II which confirms that this red object is at $z = 0.185$ and not associated with the host galaxy with redshift $z = 0.1056$ (priv comm.). For this reason, we are careful not to include this object in the photometry aperture.

PTF11mnb: The host of PTF11mnb appears to have a companion galaxy (see bottom right panel in Fig. 1.). Thus, the galaxy on the west of the image removed since the low surface brightness flux of the galaxy overlaps. Thus we use the program GALFIT (Peng et al. 2002) to model and subtract any contaminating objects from the image and then use the procedure outlined in Section 3.2 to perform aperture photometry on the galaxy.

3.3.2 Foreground star contamination

ASAS-SN 14dq: This system is a large and extended object. There are many foreground stars in this image which have been subtracted.

ASAS-SN 16al: There is a very bright star (BD-12 4185, $m_V \sim$

9.8) in the nearby field, causing large variations in the sky background. In addition, this object is aligned with many foreground stars which contribute to around 50 per cent of the light from the galaxy aperture. We modelled and subtracted these stars from images, but accurate photometry of the galaxy remains difficult. Thus we estimate the uncertainty in the removal of the foreground stars and incorporate an extra photometric error of 0.1 magnitudes into the photometry measurements.

ASAS-SN 16ns: This system has a bright ($m \sim 17$ mag) foreground star which masks a large percentage of the galaxy flux due to the small and low surface brightness nature of the galaxy. We remove this star, but the subtraction residuals remain at approximately ~ 10 per cent of the object flux in the i and z bands. Photometric uncertainties were increased accordingly.

ASAS-SN 17oj: We remove foreground stars from this image. This is a low surface brightness galaxy, so a large aperture was used to incorporate the flux in the outskirts of the galaxy.

3.3.3 Active Galactic Nuclei

We checked if any of the host galaxies in our sample had an observable AGN present. First, we inspected the SDSS spectra where available (29/84 galaxies) and used the line ratio $[\text{N II}]6583/\text{H}\alpha$ to identify the presence of an AGN (Carter et al. 2001). If $\log([\text{N II}]6583/\text{H}\alpha) > -0.25$, we assumed the spectrum could be dominated by an AGN. According to this metric, only ASAS-SN 14de (SN Ic) hosts an (observable) AGN ($\log([\text{N II}]6583/\text{H}\alpha) = -0.32$); strong $[\text{O III}]$ emission confirms it as a Seyfert 2 galaxy. While visual inspection of the host galaxy suggests that the AGN is unlikely to contribute significantly to the optical flux measured in SDSS/PS1, it could contribute more significantly to the mid-IR flux, which could in turn affect the SED derived parameters including ages of the stellar populations, star-formation rates and also dust attenuation in the host galaxy. Hence, for 14de we exclude NIR photometry for the SED fit.

Since we do not have spectra for every galaxy in our sample, we also inspected the images of each host (see Fig. 1) to check for a clear point source. Almost all galaxies are well resolved and few show a clear central point source (much less a photometrically-dominant AGN). However, the following sources in Fig. 1 do seem to have a red point source located at the centre of the host which could be either a galaxy bulge or an AGN: 14de (a seyfert galaxy), 14di, 14dl, 14kg, 16am, 16go, 17br and 17cl.

We also check the ALLWISE colours (W1–W2 and W3–W2) of the host galaxies as another diagnostic to test whether an AGN is present Wright et al. (see Fig. 12. 2010). Aside from 14de, we find that two galaxies (15fi and 14ma) have WISE colours suggestive of a possible AGN. ASAS-SN 15fi (Mrk 0884) has an SDSS spectra and we find a ratio of $\log([\text{N II}]6583/\text{H}\alpha) = -1.13$, therefore we estimate the maximum contribution to be ~ 15 per cent and we obtained a spectrum of ASAS-SN 14ma in Taggart et al (in prep) from the WHT and we find $\log([\text{N II}]6583/\text{H}\alpha) = -0.83$ indicating that AGN contribution is minimal in these host galaxies.

3.4 Literature Photometry

Photometry of SLSN and LGRB hosts was gathered primarily from the published literature. For clarity, all sources are listed in Tables D2–4 and are available in a machine readable form. If uncertainties are not given in the photometry from the literature, it is assumed that they are negligible and we therefore assign an uncertainty of 0.01 when doing the SED modelling.

We omit photometric data points in the literature if they are inconsistent with the other photometric points at nearby wavelengths at high significance, if there may be contamination from the transient given the time the data were taken, or (in cases where contamination with other galaxies is possible) if it is unclear whether the authors took deblending into account with their photometry.

3.5 New LGRB host photometry

We supplement the LGRB photometry from the literature with new photometry from a variety of sources, detailed below. A summary of our photometry is presented in Table 4.

3.5.1 Spitzer / IRAC

Most of the LGRB hosts in our sample were observed using the Infrared Array Camera (IRAC; Fazio et al. 2004) on the *Spitzer Space Telescope* (Werner et al. 2004) as part of the extended *Swift/Spitzer* Host Galaxy Legacy Survey (SHOALS; Perley et al. 2016a). These observations were generally carried out in channel 1 ($3.6\ \mu\text{m}$) only, although LGRB 060218 was also observed in channel 2 ($4.5\ \mu\text{m}$). We used the PBCD images from the *Spitzer* Heritage Archive and photometric techniques detailed in Perley et al. (2016b), including subtraction of all neighbouring objects that might contaminate the aperture or sky background. Data from some archival programs were also reanalysed using a consistent methodology. In most cases this was straightforward. In the case of LGRB 020903, isolating the host galaxy is challenging due to the presence of a dense group of merging galaxies with complicated light profiles in the foreground. The dwarf host of LGRB 130702A is part of a smaller and more distant galaxy group (Kelly et al. 2013). The companion spiral is approximately 6 magnitudes brighter and offset by 6.5 arcsec; subtraction of its halo also leaves some residuals in the sky background. As a result, in both these cases the uncertainty on the host flux is relatively large.

3.5.2 Keck / MOSFIRE

LGRB 130702A was observed in imaging mode using the Multi-Object Spectrograph for Infrared Exploration (MOSFIRE; McLean et al. 2010, 2012) at Keck Observatory on the night of 2014 Jun 16 in the J and K_s filters. We reduced these data using a custom pipeline. The resolution of these images (and of archival optical data) are sufficient that there are no issues with background contamination from the nearby galaxies. Aperture photometry is performed in a standard fashion using nearby 2MASS standards.

3.5.3 Palomar / WIRC

LGRB 120422A was observed with the Wide-Field Infrared Camera (WIRC; Wilson et al. 2003) on the Palomar 200-inch Hale telescope on the night of 2013 Feb 17 in the J and K_s filters. We reduced these data using our custom pipeline, which includes cleaning of noise signatures associated with the replacement-detector. Aperture photometry is performed in a standard fashion using nearby 2MASS standards.

3.5.4 Palomar / P60

LGRB 150818A was observed extensively with the CCD imager on the Palomar 60-inch robotic telescope (Cenko et al. 2006) as part of

Table 4. New LGRB host galaxy photometry.

LGRB	Filter	AB Mag	Instrument	Date
020903	3.6 μ m	22.30 \pm 0.30	<i>Spitzer</i> /IRAC	2006-06-07
030329A	3.6 μ m	23.71 \pm 0.11	<i>Spitzer</i> /IRAC	2017-03-31
031203	3.6 μ m	18.19 \pm 0.01	<i>Spitzer</i> /IRAC	2005-11-29
060218	3.6 μ m	20.77 \pm 0.02	<i>Spitzer</i> /IRAC	2012-11-07
	4.5 μ m	21.06 \pm 0.05	<i>Spitzer</i> /IRAC	2012-11-07
060614	3.6 μ m	22.96 \pm 0.10	<i>Spitzer</i> /IRAC	2012-11-25
080517	<i>J</i>	16.90 \pm 0.14	2MASS	-
	<i>H</i>	17.12 \pm 0.24	2MASS	-
	<i>K_s</i>	16.87 \pm 0.21	2MASS	-
111225A	3.6 μ m	24.00 \pm 0.30	<i>Spitzer</i> /IRAC	2016-12-05
120422A	3.6 μ m	21.12 \pm 0.03	<i>Spitzer</i> /IRAC	2017-02-21
	<i>J</i>	20.34 \pm 0.09	P200/WIRC	2013-02-17
	<i>K_s</i>	20.35 \pm 0.17	P200/WIRC	2013-02-17
130702A	<i>J</i>	22.63 \pm 0.17	Keck/MOSFIRE	2014-06-16
	<i>K</i>	21.41 \pm 0.45	Keck/MOSFIRE	2014-06-16
	3.6 μ m	23.80 \pm 0.30	<i>Spitzer</i> /IRAC	2016-11-05
150518A	<i>u'</i>	22.78 \pm 0.03	KeckI/LRIS	2016-06-07
	<i>g'</i>	22.07 \pm 0.14	PS1	-
	<i>r'</i>	21.43 \pm 0.08	PS1	-
	<i>i'</i>	21.25 \pm 0.13	PS1	-
	<i>z'</i>	20.65 \pm 0.11	PS1	-
	<i>y'</i>	20.80 \pm 0.34	PS1	-
	<i>J</i>	19.78 \pm 0.03	Magellan/FourStar	2016-03-27
150818A	<i>g'</i>	22.30 \pm 0.16	P60	2016-02-14
	<i>r'</i>	22.10 \pm 0.20	P60	2016-02-14
	<i>i'</i>	21.70 \pm 0.20	P60	2016-02-14
	<i>z'</i>	> 21.30	P60	2016-02-14
	3.6 μ m	21.89 \pm 0.05	<i>Spitzer</i> /IRAC	2017-02-03
161219B	3.6 μ m	20.70 \pm 0.02	<i>Spitzer</i> /IRAC	2018-01-04

Notes. Photometry is not corrected for Galactic foreground extinction. Upper limits are 2σ . All photometry is available online in a machine-readable form.

a campaign to follow-up the supernova associated with this event (Sanchez-Ramirez et al., in prep.). A series of late-time reference images in *griz* filters were taken on 2016 February 14 for the purposes of galaxy subtraction against the earlier supernova imaging; we employ these here to measure the host flux in these bands.

3.5.5 Keck / LRIS

LGRB 150518A was observed in imaging mode with LRIS (Oke et al. 1995) in the *u*-band filter on 2016 June 07. The observations were reduced with LPipe (Perley 2019) and aperture photometry of the host galaxy was measured relative to SDSS secondary standards in the field.

3.5.6 Magellan / FourStar

We observed LGRB150518A in *J*-band with the near-infrared (NIR) camera FourStar (Persson et al. 2013) at the 6.5-m Magellan/Baade telescope (Las Campanas Observatory, Chile) on 2016 March 27 as a part of the programme CN2016A-108. The observation sequence consisted of 39 dithered images with individual integration time of 32 s. The data were reduced with the software package THELI version 2.10.0 (Erben et al. 2005; Schirmer 2013).

3.6 CCSN distances

We do not have spectroscopy for each CCSN host galaxy. Thus, we obtain distances to each galaxy from redshift measurements

Table 5. New PTF SLSN host photometry.

PTF ID	Filter	AB Mag	Instrument
PTF09q	<i>u'</i>	18.20 \pm 0.08	SDSS
	<i>g'</i>	17.13 \pm 0.05	PS1
	<i>r'</i>	16.54 \pm 0.04	PS1
	<i>i'</i>	16.14 \pm 0.03	PS1
	<i>z'</i>	15.98 \pm 0.03	PS1
	<i>y'</i>	15.74 \pm 0.06	PS1
PTF10gzb	<i>u'</i>	21.10 \pm 0.22	SDSS
	<i>g'</i>	20.14 \pm 0.07	PS1
	<i>r'</i>	19.85 \pm 0.07	PS1
	<i>i'</i>	19.70 \pm 0.09	PS1
	<i>z'</i>	19.38 \pm 0.12	PS1
	<i>y'</i>	19.89 \pm 0.32	PS1
PTF11mnb	<i>u'</i>	20.42 \pm 0.08	SDSS
	<i>g'</i>	19.42 \pm 0.02	PS1
	<i>r'</i>	19.27 \pm 0.02	PS1
	<i>i'</i>	18.96 \pm 0.02	PS1
	<i>z'</i>	18.88 \pm 0.03	PS1
	<i>y'</i>	18.91 \pm 0.07	PS1
PTF12gty	<i>u'</i>	> 21.14	SDSS
	<i>g'</i>	> 23.79	PS1
	<i>r'</i>	> 23.83	PS1
	<i>i'</i>	23.78 \pm 0.24	PS1
	<i>z'</i>	22.53 \pm 0.21	PS1
	<i>y'</i>	> 23.84	PS1
PTF12hni	<i>u'</i>	20.16 \pm 0.20	SDSS
	<i>g'</i>	19.19 \pm 0.01	PS1
	<i>r'</i>	18.94 \pm 0.03	PS1
	<i>i'</i>	18.86 \pm 0.02	PS1
	<i>z'</i>	18.56 \pm 0.04	PS1
	<i>y'</i>	18.50 \pm 0.10	PS1

Notes. Photometry are not corrected for Galactic foreground extinction. Upper limits are 3σ . All photometry is available online in a machine-readable form.

as published in the NASA Extra-galactic Database (NED; <https://ned.ipac.caltech.edu/>) where available (60/84 galaxies). Since our CCSN sample are located in very low-redshift galaxies (median luminosity distance \sim 70 Mpc and all galaxies $<$ 400 Mpc), they have peculiar velocities relative to the motion due to the isotropic expansion of the Universe as described by the Hubble Flow. The fractional distance errors from peculiar velocities could have implications for the analysis of our hosts. Thus, we correct for peculiar velocity using the velocity field model in Mould et al. (2000). This model accounts for peculiar velocities due to the Virgo Cluster, the Great Attractor and the Shapley Supercluster and is typically a 6–8 per cent correction. If a catalogued redshift is not available for the host galaxy (24/84), we adopt the redshift of the SN, since the supernova redshift is a good estimator of the host galaxy redshift (Fremling et al. 2019). We estimate the uncertainty based on data from the Bright Transient Survey Fremling et al. (2019) which finds the standard deviation of the derived supernova redshift versus the host galaxy redshift to be 0.005.

4 PHYSICAL PARAMETERS

4.1 Spectral Energy Distribution Fitting

To quantify stellar parameters of the host galaxies including stellar mass and star-formation rate, we model the galaxy spectral energy distribution (SED) using UV through NIR photometry. We use the

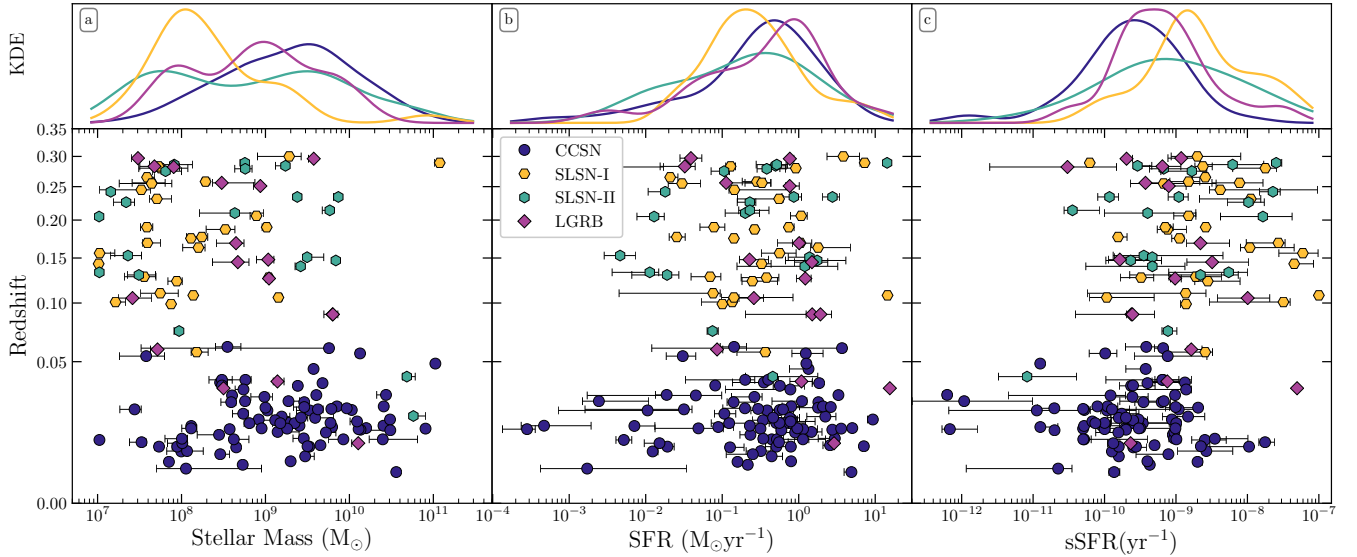


Figure 2. Distribution of the physical properties plotted against redshift for each host galaxy sample. Panel (a) shows the stellar mass, (b) star formation rate, and (c) specific star formation rate all plotted against redshift using a square root scale. Each upper panel is a Gaussian kernel density estimation of each physical property. Redshift evolution is not corrected for in the physical parameters.

code LEPHARE⁵ (Ilbert et al. 2006) which uses single-age stellar population synthesis model templates of Bruzual & Charlot (2003) summed according to a single-burst of exponentially declining star-formation. We assume a Chabrier initial mass function (Chabrier 2003) and a stellar metallicity set between 0.2–1.0 Z_{\odot} . The contribution of emission lines to the modelled spectra is based on the Kennicutt (1998) relations between SFR and UV luminosity. The contribution of H α and [O II] lines to the photometry is included for galaxies with dust free colour bluer than $(NUV-r)_{\text{ABS}} \leq 4$ and the intensity of the emission lines is scaled according to the intrinsic UV luminosity of the galaxy. Dust attenuation in the galaxy is applied to the SED models using the Calzetti et al. (2000) extinction law for starburst galaxies. Where spectroscopy of the host galaxy is available and shows little evidence for nebular emission, we fit a continuum driven SED.

To calculate the uncertainties involved in deriving the mass and star-formation rate parameters we perform a simple Monte Carlo analysis. We choose a random number from a Gaussian distribution in flux space with standard deviation equal to the photometric uncertainty on the derived magnitude for each filter and for each host. We sample from the distribution 1000 times and then run the SED fit on each set of ‘noisy’ photometry and use the 1σ uncertainties. If the reduced $\chi^2 \gg 1$ (before the Monte Carlo sampling) and the SED photometry is well-sampled in the UV, optical and mid-IR, we apply additional uncertainty to the photometry equally across all photometric points before the Monte Carlo sampling in order to better fit the data until the reduced chi-squared is approximately one and then re-run the Monte Carlo sampling.

A polycyclic aromatic hydrocarbon (PAH; Leger & Puget 1984) emission feature is present within the *WISE* W1/*Spitzer* 3.6 μm bands at $z < 0.2$. In most galaxies this emission is insignificant compared to the stellar continuum. However, in low-mass galaxies with extreme star-formation, this non-stellar feature can significantly contribute to the flux in the near-IR. LEPHARE does

not account for this emission feature. Thus we investigate if there is any evidence that this feature at 3.6 μm may affect the flux in this band. One case where this might be significant for the host of LGRB 031203. However, Watson et al. (2011) studied the mid-infrared spectrum and do not find any evidence for PAH emission in the host of LGRB 031203.

4.2 Redshift evolution correction

While we have restricted all our samples to relatively low-redshift, Fig. 2 shows clearly that there are still redshift differences between our samples—in particular, between the CCSNe (nearly all at $z \sim 0$) and the more extreme supernovae for which our ultimate goal is to compare (typically at $z \sim 0.2$). The overall SFR density of the Universe, and of individual galaxies, rises rapidly with increasing redshift (e.g. Lilly et al. 1996), making it likely that the rare, luminous SNe that are typically found at higher redshifts than common, less luminous SNe will tend to be found in galaxies with higher star-formation rates simply on account of the effects of cosmic evolution.

To make a direct comparison between our samples and to avoid systematic errors introduced by cosmic evolution we correct for redshift evolution in SFR by empirically re-scaling all star formation rates to $z = 0$. We do this by measuring the ratio between the SFR expected for a $z = 0$ galaxy on the main-sequence (for the specific host galaxy stellar mass) versus the expected SFR for this galaxy at the redshift of the host $\text{SFR}_{\text{MS}(M,0)} / \text{SFR}_{\text{MS}(M,z)}$. We use this ratio to scale the measured SFR and sSFR down to $z = 0$ as in Eq. 1.

$$\text{SFR}_{\text{corrected}} = \text{SFR}_{\text{measured}} \frac{\text{SFR}_{\text{MS}(M,0)}}{\text{SFR}_{\text{MS}(M,z)}} \quad (1)$$

⁵ <http://www.cfht.hawaii.edu/arnouts/LEPHARE/lephare.html>

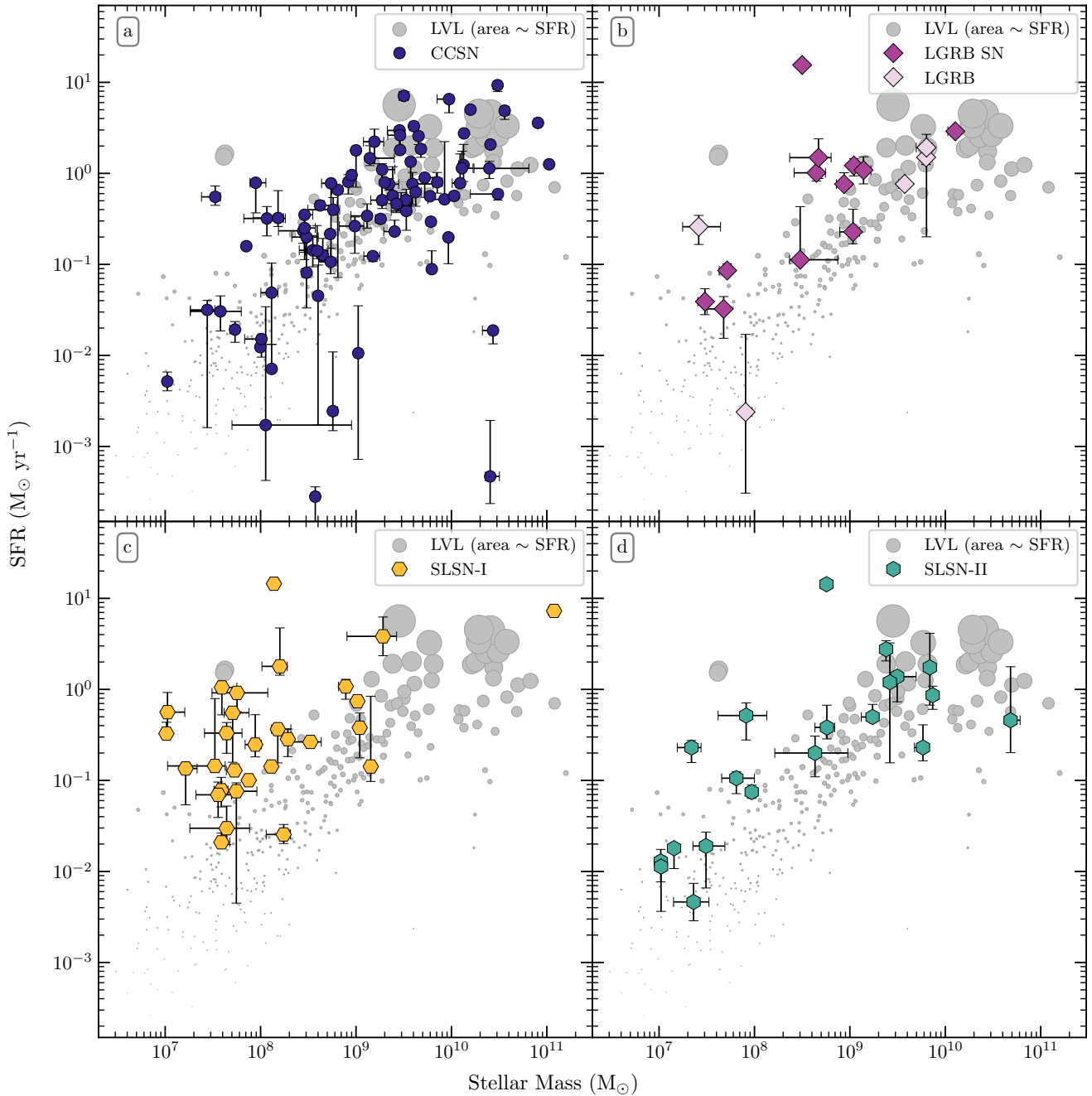


Figure 3. Star formation rate vs. stellar mass for each transient hosting galaxy class. SFR has not been corrected for redshift evolution. Grey points are the LVL survey galaxies with their sizes scaled in proportion to SFR to show the probability of producing a SN per unit time. Panel a shows the unbiased CCSN sample in blue. Panel b shows the LGRB sample in purple; the darker shade indicates where the LGRB was associated with a SN or optical afterglow. Panel c shows the SLSN-I sample. Panel d shows the SLSN-II sample. CCSN hosts are found in similar environments to the scaled local galaxies in the LVL survey.

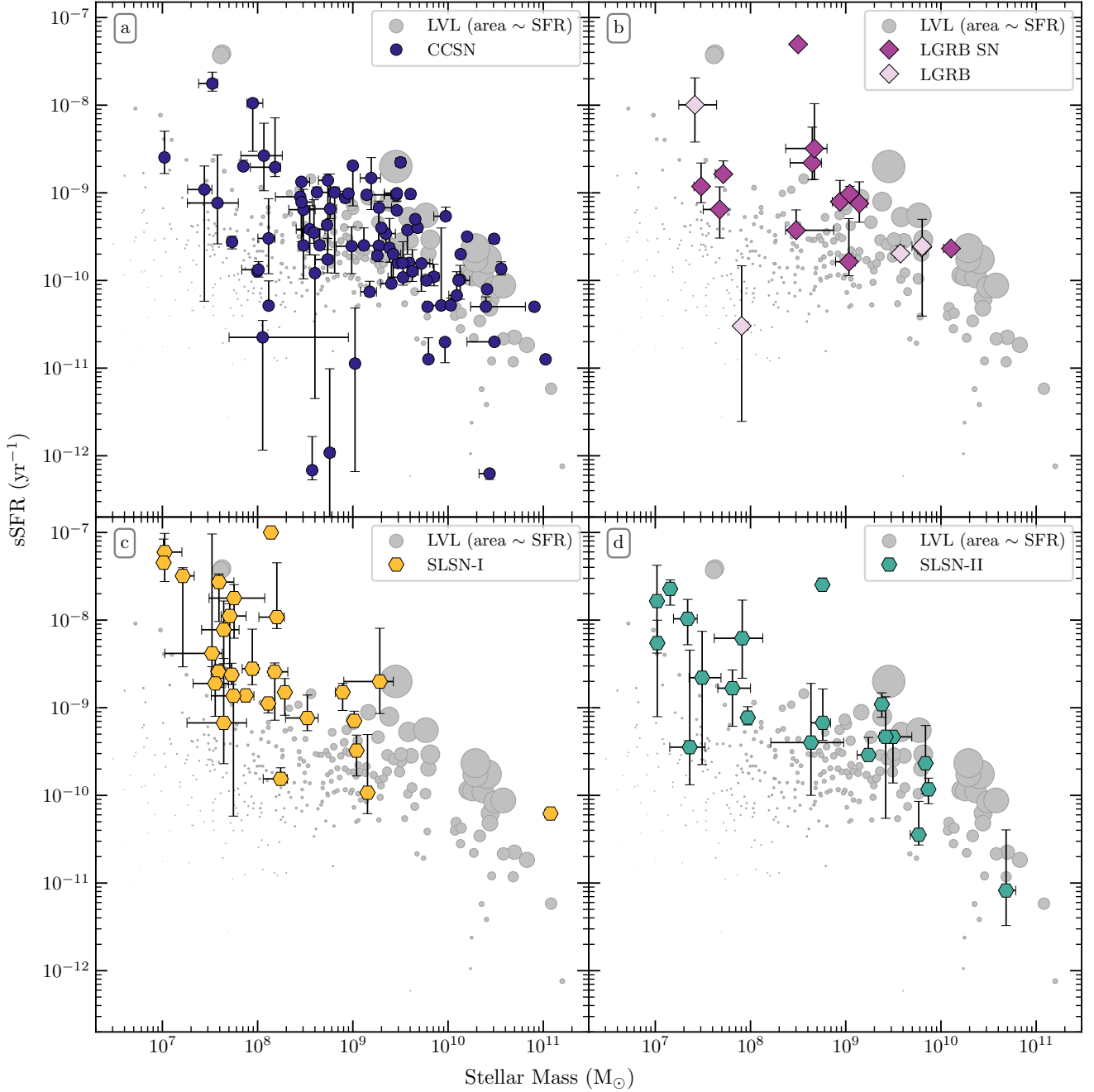


Figure 4. Specific star formation rate vs. stellar mass. As in previous figure, SFRs have not been corrected for redshift evolution. The symbols and colours are the same as in Fig. 3. SLSN-I show a strong preference for galaxies with high sSFR, low stellar mass, (top left of the diagram), whereas CCSN are consistent with the distribution of LVL galaxies and are found primarily in the bottom right of the plot. SLSN-II and LGRB hosts seem roughly consistent with the CCSN, though in both cases there are a higher fraction on the top left compared to the CCSN.

Table 6. Statistical properties of galaxy samples. 10th, 50th(median) and 90th percentiles are given for each physical parameter. 1σ uncertainties are given on the median derived parameters. Star-formation rates are not corrected for redshift evolution.

		z			$\log_{10}M_*$ (M_\odot)			$\log_{10}\text{SFR}$ ($M_\odot\text{yr}^{-1}$)			$\log_{10}\text{sSFR}$ (yr^{-1})			$\log_{10}(\Delta S)$		
Transient	N	10	50	90	10	50	90	10	50	90	10	50	90	10	50	90
CCSN	84	0.007	0.016	0.036	8.0	9.3(0.1)	10.3	-1.8	-0.3(0.1)	0.4	-10.7	-9.6(0.1)	-8.8	-0.7	0.0(0.1)	0.7
SLSN-I	29	0.105	0.177	0.281	7.5	7.9(0.2)	9.1	-1.2	-0.5(0.2)	0.3	-9.6	-8.6(0.1)	-7.5	-0.3	0.3(0.1)	1.3
SLSN-II	21	0.074	0.210	0.284	7.2	8.8(0.5)	9.9	-1.9	-0.6(0.3)	0.2	-10.4	-9.2(0.3)	-7.8	-0.8	-0.1(0.1)	0.8
LGRB SN	12	0.033	0.146	0.280	7.7	8.7(0.2)	9.1	-1.4	-0.1(0.3)	0.4	-9.6	-9.1(0.1)	-8.5	-0.2	0.3(0.2)	0.8
SN-less LGRB	5	0.089	0.105	0.290	7.6	9.6(0.9)	9.8	-1.8	-0.1(0.6)	0.2	-10.2	-9.6(0.4)	-8.6	-1.0	0.1(0.5)	0.7

We parameterise the main-sequence as a power-law, as in Eq. 2.

$$\text{SFR}_{\text{MS}} = \text{SFR}_0 \left(M_*/10^{10} M_\odot \right)^\alpha \quad (2)$$

Parameter (α) is the slope of the galaxy main-sequence and (SFR_0) describes the normalisation at a stellar mass of $10^{10} M_\odot$, which varies as a function of redshift. Parameters were derived from observational data in [Salim et al. \(2007\)](#) ($z \sim 0.1$) and [Noeske et al. \(2007\)](#) ($z \sim 0.36$). The approximate values are ($\text{SFR}_0 / M_\odot \text{yr}^{-1}$, α) = (1.48, 0.65) for the galaxy main-sequence at $z \sim 0.1$ and (2.3, 0.67) for $z \sim 0.36$. We interpolate these parameters (α and SFR_0) over the redshift range of our sample in order to calculate the SFR of a main sequence galaxy (with a certain stellar mass) at every host redshift and at redshift zero.

We apply this correction to the sSFR and SFR when we statistically compare the host galaxy populations of CCSNe, SLSNe and LGRBs. Once these corrections are applied, we find the median SFR is reduced by 0.01 dex for CCSN, 0.42 dex for SLSN-I, 0.15 dex for SLSN-II and 0.20 dex for LGRBs. Parameters have not been corrected, unless specifically indicated in the text and figure caption. We provide the derived physical parameters from SED fits without applying this SFR correction in Tables B1–B3.

4.3 Sequence-offset parameter

As an alternative to applying a redshift evolution correction to the SFR to deal with cosmic evolution, we also define an alternative metric of star-formation intensity, the ‘sequence-offset’ parameter (ΔS). This parameter, given by Eq. 3, measures the ratio between the actual, SED-measured star formation rate of a galaxy in our sample (SFR_{host}) vs. the predicted SFR (SFR_{MS}) for a galaxy on the star-forming galaxy main-sequence at the same redshift with the same stellar mass, based on the main sequence parametrisation in Eq. 2.

$$\Delta S = \text{SFR}_{\text{host}}(M_*, z) / \text{SFR}_{\text{MS}}(M_*, z) \quad (3)$$

5 RESULTS

In this section we present the integrated galaxy properties derived from the SED fitting for nearby SLSN, LGRBs and the ASAS-SN CCSN. Basic statistical properties of each sample are summarised in Table 4.1. Uncertainties (1σ) are calculated using a simple bootstrap.

5.1 Basic properties of CCSN hosts and comparisons to nearby star-forming galaxies

A key goal of our study is to produce a uniform and unbiased sample of CCSN hosts, providing a galaxy-luminosity-independent tracer of the sites of star-formation in the local universe. While our primary motivation for this exercise will be to compare this sample to ‘exotic’ supernova types (SLSNe and LGRBs) in order to constrain their progenitors, our CCSN sample is also useful for studying the nature of star-formation at low-redshift: few galaxy surveys are complete beyond the dwarf galaxy $\lesssim 10^9 M_\odot$ limit, and those that are are typically confined to small volumes limited by cosmic variance.

In Fig. 3a, we present the distribution of SFR vs. stellar mass for core-collapse SNe as compared to galaxies from the Local Volume Legacy Survey (LVLS). The LVLS is a volume-complete sample of galaxies within ~ 11 Mpc, with stellar masses derived from SED fits (Johnson et al. in prep) and star formation rates derived from $\text{H}\alpha$ flux ([Lee et al. 2011](#))⁶. Most LVLS galaxies are observed to populate the main sequence of star-forming galaxies, where mass and star-formation rate are strongly correlated in a fairly narrow band of specific star-formation rate between 10^{-9} – 10^{-10} yr^{-1} .

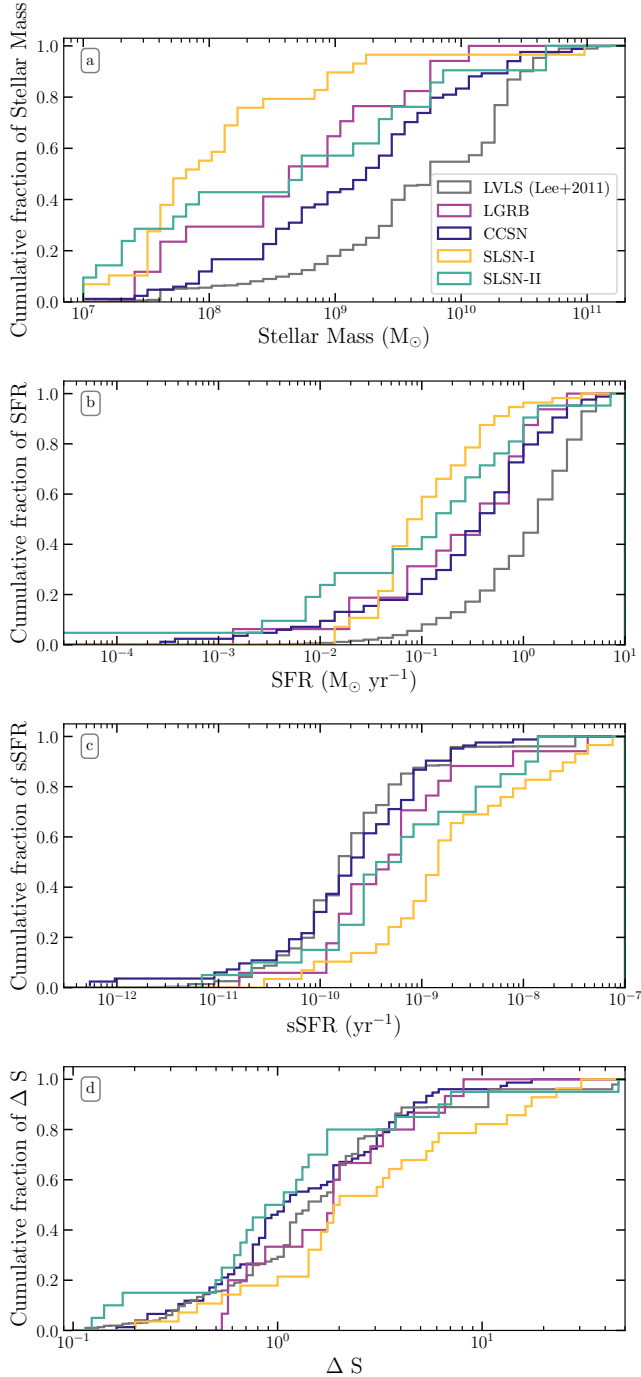
As expected, CCSNe also populate star-forming galaxies across a large mass distribution—probing large spiral galaxies with stellar masses $\sim 10^{11} M_\odot$ down to the low-mass dwarf galaxy regime with stellar masses of $\sim 10^7 M_\odot$. However, the mass distributions are not strictly identical: the median SFR-weighted log stellar mass of LVLS galaxies is 9.8(0.1), 0.5 dex lower than the median mass of CCSN hosts 9.3(0.1) (The associated Anderson-Darling p -value is $p_{\text{AD}}=3e-04$). This may be associated with cosmic variance effects in the small LVLS volume (e.g., an overabundance of large galaxies due to large-scale structure) and demonstrates the importance of obtaining a sample selected via SNe. Similar small but statistically significant differences are also seen in other parameters (SFR, sSFR, and sequence offset).

A few CCSN galaxies in Fig. 3a show very low star-formation rates despite high masses – specifically 14de and 16am. Morphologically, these galaxies are not classical spiral galaxies, neither are they elliptical galaxies. These galaxies do have red colours and the uncertainties on the SFRs derived for these galaxies are likely under-estimated by our SED fitting procedure at minimum.

The fraction of star-formation in very faint or very rare galaxies that are poorly probed by traditional flux- or volume-limited galaxy surveys is of particular interest. Using our sample, we measure the fraction of CCSNe in dwarf galaxies and the fraction in

⁶ Note that this SFR indicator is different from the one employed in our SED analysis; we provide it as a visual comparison indicator and because it has been employed as the comparison sample in earlier transient host studies (in particular, [Perley et al. 2016c](#)). We also statistically compare the LVLS vs. CCSN sample using both $\text{H}\alpha$ and UV SFRs.

Figure 5. Cumulative distributions of the different galaxy samples with colours the same as in previous figures. We empirically re-scale all star formation rates to $z = 0$ for all host galaxy samples (CCSNe, SLSNe-I, SLSNe-II and LGRBs) using the procedure in 4.2. The LVLS galaxies (in grey) are weighted here by SFR (step size) to create a galaxy population that traces star-formation. Panel a: cumulative distributions of all galaxy populations by mass. Panel b: cumulative distributions of all galaxy populations by star-formation rate. Panel c & Panel d show measures of star-formation intensity via sSFR and sequence offsets from star-formation rate compared with the galaxy main sequence at that redshift. CCSN and the weighted LVLS are similar, although not identical.



‘starburst’ galaxies. We use Bayesian beta distribution quantile technique to derive the 1- σ uncertainties following methods outlined in Cameron (2011). We find 40^{+6}_{-5} per cent of CCSNe (34/84 from our sample) occur in dwarf galaxies with stellar masses less than $10^9 M_\odot$ and 10^{+4}_{-2} per cent of CCSNe (8/84 from our sample) occur in dwarf galaxies with stellar masses less than $10^8 M_\odot$. These fractions are substantial, emphasising the importance of dwarf galaxies to cosmic evolution. However, only 2^{+3}_{-1} per cent (2/84) of CCSN hosts are undergoing very rapid star-formation in a starburst galaxy ($sSFR > 10^8 \text{ yr}^{-1}$), all of which are dwarf galaxies. Thus, we find the vast majority of star-formation in the local Universe does not occur in starbursting galaxies. This is in agreement with the LVLS survey Lee et al. (2009) which found only a few per cent of the galaxies are now in a bursting mode (defined in their analysis as a $H\alpha$ equivalent width > 100) and in Brinchmann et al. (2004) where it is estimated that ~ 20 per cent of local star-formation occurs in starburst galaxies.

5.2 Basic properties of exotic SN hosts

In Fig. 3b-d we also plot the mass and SFRs of the ‘exotic’ SN samples in comparison to local galaxies. These populations are clearly quite different from ordinary CCSNe. The peak of the SLSN-I host mass distribution is much lower than the CCSN population, with a median log stellar mass of 7.9(0.2), though notably, there are a few outliers in galaxies with masses exceeding relatively high masses (PTF10uhf, 2017egm and PTF09q). SLSN-II and LGRBs with observed associated SNe lie intermediate between the SLSN-I and CCSN samples with median masses 8.8(0.5) and 8.7(0.2) respectively (SN-less LGRBs have masses more consistent with CCSN with a median stellar mass of 9.6(0.9), although this is poorly constrained).

Unlike CCSNe, SLSN and LGRBs frequently populate galaxies above the galaxy main sequence with median sSFR of -8.6(0.1) (SLSN-I), -9.2(0.3) (SLSN-II) and -9.1(0.1) (LGRB SN). Again, SN-less LGRBs have sSFR of -9.6(0.4) which is more consistent with the CCSN. This effect can be seen more clearly in Fig. 4, which shows specific star formation vs. stellar mass. The impartially selected CCSNe are consistent with star-forming local galaxies, whereas ~ 70 per cent of SLSN-I lie above the star-forming galaxy main sequence with specific star-formation rates exceeding 10^{-9} yr^{-1} . This places many SLSN-I hosts in the top left of this diagram, with 8 hosts with specific star formation rates exceeding 10^{-8} yr^{-1} , which is much more than expected if the SLSN rate purely traces SFR (which has also been noted by others; e.g., Lunan et al. 2014; Perley et al. 2016c; Schulze et al. 2018). These galaxies (with specific star formation significantly above this main sequence) are sometimes referred to as starbursts. There are 8 (~ 30 percent) SLSN-I galaxies with specific star formation rates exceeding 10^{-8} yr^{-1} (which we will define as a ‘starburst’ for the purpose of this paper). This is in qualitative agreement with other studies, such as in Leloudas et al. (2015) where ~ 50 per cent of SLSN-I were found in EELGS indicative of an intense starburst episode within the galaxy. Perley et al. (2016c) and Schulze et al. (2018) also noted that many SLSN-I host galaxies in PTF and SUSHIES samples are undergoing intense star-formation.

5.3 Relative Rates of SN Subtypes

While we can qualitatively observe that the distributions of certain samples in Fig. 2–4 seem similar or dissimilar, this is not a statistical statement. We employ several different methods to quantify

Table 7. Two sample Anderson-Darling probabilities between CCSNe and other galaxy samples (SLSNe-I, SLSNe-II, LGRB-SNe and SN-less LGRBs) and between LGRBs with and without supernova. We empirically re-scale all star formation rates to $z=0$ for all host galaxy samples (CCSNe, SLSNe-I, SLSNe-II and LGRBs) using the procedure in 4.2. Samples that differ at $p < 0.05$ for that parameter are in boldface.

Parameter	Comparison	p -value
Mass	CCSN-LVLS	3.23e-04
	CCSN-SLSN-I	8.90e-06
	CCSN-SLSN-II	1.52e-02
	CCSN-LGRB SN	3.74e-02
	CCSN-SN-less LGRB	0.36
	LGRB SN-SN-less LGRB	0.29
SFR	CCSN-LVLS (UV)	1.27e-03
	CCSN-SLSN-I	1.50e-04
	CCSN-SLSN-II	9.66e-02
	CCSN-LGRB SN	0.72
	CCSN-SN-less LGRB	0.87
	LGRB SN-SN-less LGRB	0.81
sSFR	CCSN-LVLS (UV)	2.65e-02
	CCSN-SLSN-I	1.03e-05
	CCSN-SLSN-II	3.18e-02
	CCSN-LGRB SN	2.20e-02
	CCSN-SN-less LGRB	0.71
	LGRB SN-SN-less LGRB	3.4e-02
Δ SFR	CCSN-LVLS (UV)	1.68e-05
	CCSN-SLSN-I	1.09e-03
	CCSN-SLSN-II	0.69
	CCSN-LGRB SN	0.14
	CCSN-SN-less LGRB	0.97
	LGRB SN-SN-less LGRB	0.50
	LGRB SN-SN-SLSN-I	0.82

the significance and model the nature of these apparent differences below.

5.3.1 Cumulative Distribution Tests

In Fig. 5., we show the cumulative distributions of mass, star-formation rate, specific star formation rate and sequence offset for each of our galaxy samples. The step size of local galaxies in LVL are weighted by star-formation to create a population consistent with one that traces star-formation. The CCSNe and LVLS samples have remarkably similar sSFR and Δ S distributions, while the rarer SN subtypes seem to show different distributions in most properties. These differences can be tested formally using Anderson-Darling tests.

We compute the Anderson-Darling (AD) statistic, and associated p -value, for each pair of samples and for each parameter of interest: stellar mass, SFR, sSFR and the sequence offset parameter (Δ S). The results are summarised in Table 7. SLSN-I are statistically distinct from the CCSN in every parameter ($p_{AD} > 0.05$): mass ($p_{AD}=9e-06$), SFR ($p_{AD}=2e-04$), sSFR ($p_{AD}=1e-05$) and Δ S ($p_{AD}=1e-03$). This population shows the most divergent properties out of all galaxy samples. SLSN-II fall intermediately between these two populations and are statistically distinct from CCSN in terms of mass ($p_{AD}=2e-02$) and sSFR ($p_{AD}=3e-02$).

5.3.2 Relative rate formalism for univariate comparisons

While the Anderson-Darling tests above confirm that differences exist between some distributions, they do not tell us anything about the degree or quantitative nature of the differences between any two distributions.

To gain further insight into the differences between the distributions of different samples, we define a new quantity which we refer to as the *relative rate* (designated \mathfrak{R}). This quantity measures how more frequent a specific type of SN (type ‘A’, typically an exotic class of SN) is compared to another type of SN (type ‘B’, typically a normal class of SN) in a specific type of galaxy, compared to the Universe as a whole. Expressed in terms of a single parameter y (which can be mass, SFR, etc.), it is the ratio of the inferred probability density functions of the two SN types:

$$\mathfrak{R}_{A/B}(y) = \frac{\text{PDF}_A(y)}{\text{PDF}_B(y)} \quad (4)$$

A relative rate $\mathfrak{R} = 1$ for all values of y would indicate that the distributions over y for A and B are identical (although the *absolute* rates may not be the same). Otherwise, regions over y with $\mathfrak{R} > 1$ indicate environments where production of SNe of type A is enhanced relative to B; regions with $\mathfrak{R} < 1$ indicate environments where production of type A is suppressed relative to B.

In practice, we use a sliding-windowed method to estimate \mathfrak{R} for each parameter of interest (stellar mass, star-formation rate, specific star-formation rate, or sequence offset). The PDF function for each parameter for each sample (A or B) is estimated by calculating the proportion P_i of host galaxies in that sample with parameter values within ± 0.5 dex of a grid of bin centres, y_i . If the number of galaxies within ± 0.5 dex of y_i is n_i and the sample size is N , this is then (for sample A):

$$P_A(y_i) = \frac{n_{A,i}}{N_A} \quad (5)$$

The (estimated) *relative* rate of one transient compared to another, $\mathfrak{R}_{A/B}$, is then the ratio of the two P arrays:

$$\mathfrak{R}_{A/B}(y_i) = \frac{P_A(y_i)}{P_B(y_i)} = \frac{n_{A,i}N_B}{n_{B,i}N_A} \quad (6)$$

The bin centres are defined in logarithmic intervals of 0.1 dex, such that every 10th window has no overlap with the first. For example, the window is evaluated between a mass of 1×10^6 to 1×10^7 (centred at 3.16×10^6), then at 1.26×10^6 to 1.26×10^7 (centred at 3.98×10^6), etc.

The beta distribution quantile technique is used to calculate confidence intervals on the relative rate function via the methods outlined in Cameron (2011). This simple Bayesian technique uses a uniform prior for the true population proportion. We use the beta distribution function as the prior probability distribution to model the behaviour of random variables. (Note that because windows within 1 dex overlap, values of \mathfrak{R} within 1 dex of each other are not fully independent.)

5.3.3 Relative rate formalism for bivariate comparisons

Testing on a single parameter at a time will not be able to distinguish between fundamental differences vs. those that originate purely due to correlations with other parameters: many galaxy parameters (e.g., SFR and stellar mass) are strongly correlated, making it difficult to tell which parameter is more directly related to

the special conditions that appear necessary for (e.g.) SLSN production.

However, our relative-rate formalism above can be extended to ascertain whether a difference in distributions associated with a control parameter (e.g. stellar mass) can completely explain an observed difference in distributions for another parameter (e.g. SFR). To test this, we *reweight* the comparison sample (sample ‘B’) according to the relative rates inferred for the control parameter using a Monte Carlo resampling procedure, and then test whether the relative rate for sample ‘A’ vs. the reweighted sample ‘B’ is consistent with a constant $\mathfrak{R}=1$ over the entire range of the test parameter.

5.4 SLSNe-I vs. CCSNe

The relative rate \mathfrak{R} of SLSNe-I vs. CCSNe is plotted in the left panels of Fig. 6, as purple dashed lines with the 2σ confidence intervals in a lighter colour against sSFR, sequence offset, redshift corrected sSFR scaled to $z \sim 0$ and stellar mass. The grey line indicates the same relative rate.

SLSN-I are strongly enhanced in galaxies with sSFR exceeding 10^{-9} yr^{-1} (after correcting for redshift evolution) and by a factor of ~ 10 for sSFR exceeding 10^{-8} yr^{-1} . The rate is also enhanced for galaxies with a sequence offset parameter exceeding 5, which corresponds to galaxies with SFR 5 times that predicted of a galaxies on the main sequence with the stellar mass and redshift of the host. The bottom left panel shows that the rate is increased for galaxies with stellar mass less than $3 \times 10^8 \text{ M}_\odot$.

To investigate whether SLSN host galaxy mass (a proxy for metallicity) or specific star formation rate (a proxy for star-formation intensity) is more closely related to the factor driving the production of these events, we must correct for the co-variation between these two parameters. As described above, we remove the effects of a possible dependence in the relative rate of SLSN to CCSN as a function of specific star formation rate by controlling for the mass dependence in order to see whether specific star formation rate alone can explain the over-abundance of SLSN-I relative to CCSN. We also do the reverse, in order to see whether a specific star formation rate dependence alone would explain the observed apparent mass dependence in the relative rate.)

The right panels of Fig. 6, show the original relative rates as a purple dashed line. The blue and red solid lines show the rates when one controls for mass dependence or sSFR dependence respectively. In each case the covariance-corrected rates level off to an equal rate (grey line), suggesting that either mass dependence or sSFR can explain the difference in relative rates between the CCSN and SLSN in our sample. As such we are unable to break the degeneracy between these parameters at present with this sample.

5.5 LGRBs vs. CCSNe

Using the same method as described above, we also calculate relative rate \mathfrak{R} of LGRBs vs. CCSNe in Fig. 7. Given the rather limited low- z LGRB sample the results are generally less constraining as for SLSNe, and we cannot conclusively (for any 1-dex bin) state that $\mathfrak{R} \neq 1$ for GRBs versus SNe given this analysis.

Formally, the relative rate of LGRBs is enhanced in galaxies with sSFRs exceeding 10^{-9} yr^{-1} (after correcting for redshift evolution) by a factor of ~ 3 ; it is enhanced in galaxies with sequence offsets > 2 by a factor of approximately 2, and it is enhanced in low-mass dwarfs $< 10^8$ by a factor of approximately 2.5. As with SLSNe, these effects are degenerate and given the small sample

sizes, we cannot yet determine which parameter (if any) is the primary cause of the differences.

5.6 SLSNe-I vs. LGRBs

We can also compare the LGRB and SLSN-I host populations directly against each other. We find that statistically they are consistent with being drawn from the same galaxy populations in terms of all measured parameters (see Table 7). This is in agreement with conclusions in Lunyan et al. (2014) who find that the stellar mass, SFR, sSFR and metallicity of SLSN-I and LGRBs are statistically indistinct below redshifts $z < 1.6$. Lunyan et al. (2014) find SLSN-I host galaxies generally exhibit lower stellar masses (with median logarithmic stellar mass ~ 8.3) compared to LGRBs, especially at low redshifts. Our results agree with these conclusions the median (with median stellar masses $7.9(0.2)$) compared to LGRB SNe (with median stellar masses $8.7(0.2)$). In terms of sSFR, our results are fully consistent with those of Leloudas et al. (2015) who found the median sSFR (SFR determined via spectroscopic line measurements) was more strongly star-forming in SLSN-I compared to LGRBs with logarithmic sSFR of -8.53 yr^{-1} for SLSNe-I and -9.15 yr^{-1} for LGRBs. We find sSFRs $-8.6(0.1) \text{ yr}^{-1}$ for SLSNe-I and $-9.1(0.1) \text{ yr}^{-1}$ for LGRB-SNe.

5.7 SN-less LGRBs vs. LGRB-SNe

To address whether the sub-population of ‘SN-less’ LGRBs may represent a distinct class from the remainder of LGRBs, we compare the host properties of the five events above to the remainder of the sample (Table 4.1). While some SN-less LGRB hosts are individually unusual, their cumulative properties are not significantly different from the hosts of LGRBs with confirmed SNe (see Table 7), although the redshift corrected sSFR may show difference ($p_{\text{AD}}=0.03$). However, this comparison is not strongly constraining given the small size of the SN-less sample (5 objects) and the possibility that some of these events hosted ordinary LGRB-SNe which were dust-obscured ⁷.

⁷ A more detailed discussion of this issue can be found in Section F.

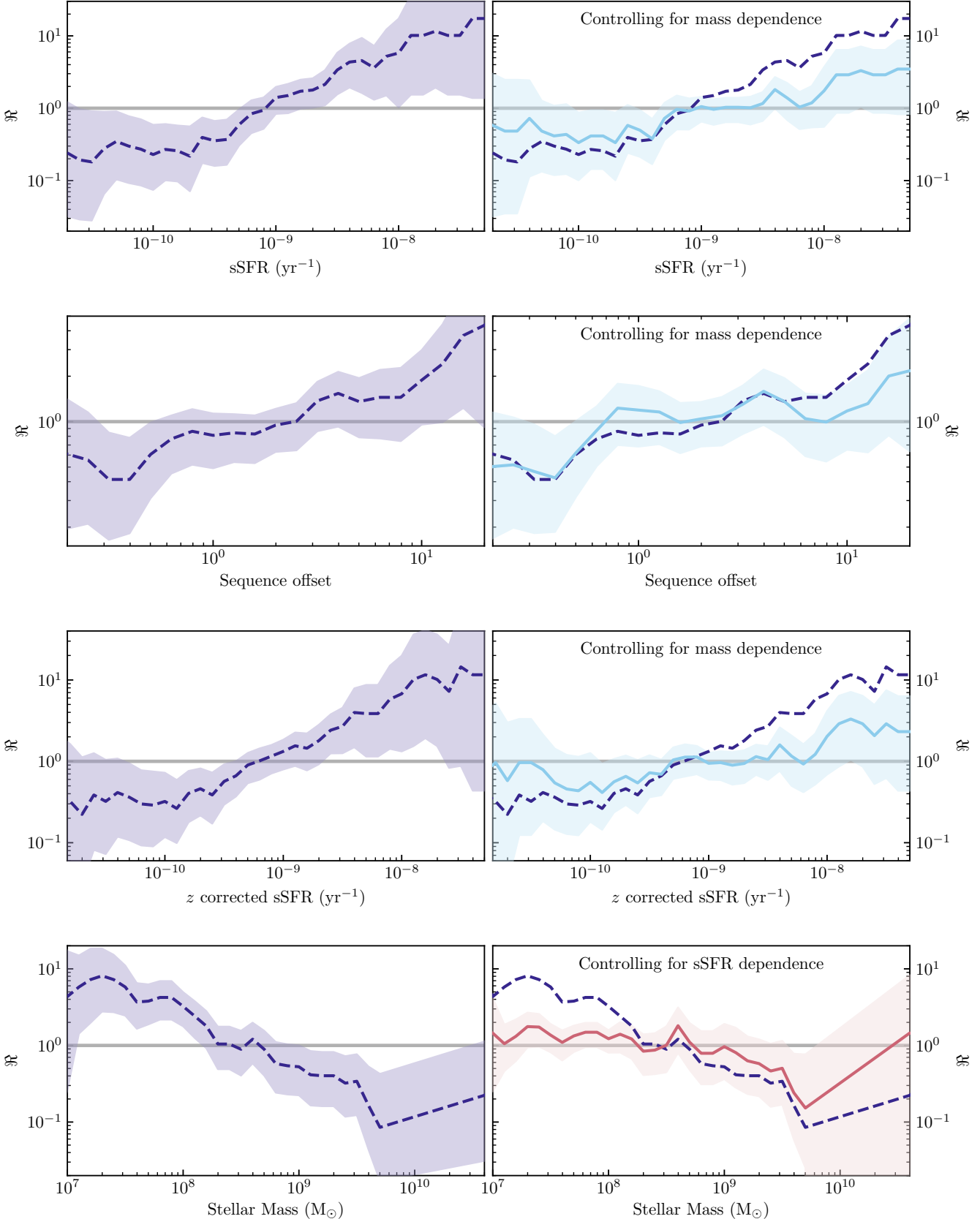


Figure 6. Relative rates of SLSN-I to CCSN for various host galaxy parameters. Left panels show the relative rates in purple given by the dashed lines for specific star formation rate, sequence offset (redshift corrected to $z \sim 0$) and stellar mass in a moving window function with a width of 1 dex. The window function moves such that after it has moved 10 times it has no overlap with the first window. 2σ confidence intervals are shown in a lighter shade. Right panels show the same quantity, but after controlling for the modeled dependence on the alternative variable (stellar mass for SFR-related quantities, or SFR for mass-related quantities). Light blue lines are mass-controlled rates and red lines are the sSFR controlled rates.

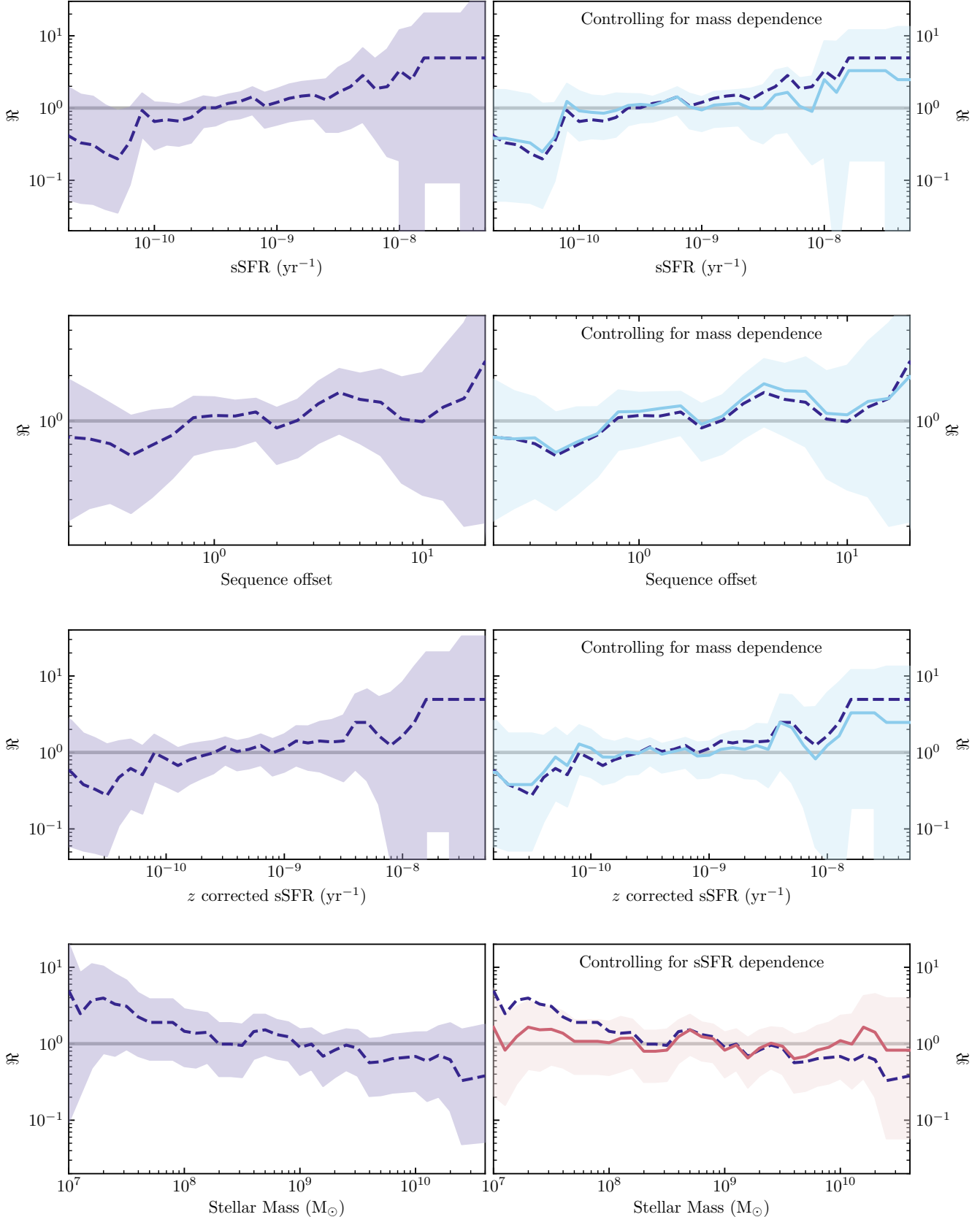


Figure 7. Relative rates of LGRB to CCSN for various host galaxy parameters. Left panels show the relative rates in purple given by the dashed lines for specific star formation rate, sequence offset (redshift corrected to $z \sim 0$) and stellar mass in a moving window function with a width of 1 dex. The window function moves such that after it has moved 10 times it has no overlap with the first window. 2σ confidence intervals are shown in a lighter shade. Right panels show the same quantities, but after for controlling for the alternative variable as in Fig. 6. Light blue lines are mass-controlled rates and red lines are the sSFR controlled rates.

6 SUMMARY AND CONCLUSIONS

In this paper we presented photometric observations of 84 galaxies hosting CCSN discovered or observed by the ASAS-SN in order to provide the most comprehensive and unbiased comparison sample of CCSN host galaxies, and compared the properties of this sample to nearby ($z < 0.3$) SLSNe, CCSNe and LGRB SN hosts. Our key conclusions are summarised as follows:

- (i) CCSNe generally exhibit similar star-formation properties to star-formation-weighted local galaxies (LVL), consistent with the expectation that CCSNe should trace star-formation. However, we find the CCSN-selected galaxy stellar mass distribution to be weighted towards slightly lower-mass galaxies (0.5 dex) than the SFR-weighted LVLS galaxy stellar mass distribution, possibly indicating that the local-volume sample is affected by cosmic variance.
- (ii) 40_{-5}^{+6} per cent of CCSNe (34/84 from our sample) occur in dwarf galaxies with stellar masses less than $10^9 M_{\odot}$ and 10_{-2}^{+4} per cent of CCSNe (8/84 from our sample) occur in dwarf galaxies with stellar masses less than $10^8 M_{\odot}$ and represent a substantial fraction of the population. This ultra-low-mass regime is one that SNe probe almost uniquely and are systematically missed by earlier, targeted searches for SN.
- (iii) Only a few per cent (2_{-1}^{+3}) of CCSN hosts are undergoing starbursts with rapid star-formation $sSFR > 10^8 \text{ yr}^{-1}$, all of which are dwarf galaxies.
- (iv) LGRB SN and SLSN-I host populations exhibit similar host galaxy properties. The peak of their host mass distributions is clearly much lower (with median logarithmic masses of 8.7(0.2) and 7.9(0.2) respectively) and spans a much smaller mass range than the CCSN population (with median logarithmic mass of 9.3(0.1) which trace star-formation. LGRB SN explode, on average, in higher mass galaxies than SLSNe-I. This lends further support to models in which LGRBs and SLSN-I form only in certain environmental conditions related to low-mass and metallicity.
- (v) We do not find statistically significant differences between LGRB-SN and SN-less LGRBs. SN-less LGRBs seem consistent with the host galaxies of the ordinary CCSN sample. However, this comparison is limited by the small sample size of SN-less events (only 5).
- (vi) Many (8/29) SLSN-I are found in starbursts. This greater fraction is consistent with an intrinsic preference for starbursting galaxies, but is also consistent with resulting purely from a strong SLSN-I mass dependence in covariance with a larger starburst fraction in dwarf galaxies. We cannot yet conclusively identify or rule out a role for intense star-formation in increasing the SLSN-I rate in starbursting dwarf galaxies.

Here we provided an unbiased sample of photometrically-derived properties of CCSN host galaxies, and directly compared them to a consistent analysis of all known SLSN and LGRB host galaxies. These catalogues are all included in a machine readable format and could be used for host preferences of events broad applicability, including unusual classes of object — such as the emerging category of fast blue transients (e.g., [Drout et al. 2014](#)).

In future work, we will increase our sample size, to try to better disentangle the role of sSFR and stellar mass in SLSN-I production. We will also gather spectroscopy of the dwarf galaxies hosting CCSN and narrow-band H α to study their chemical abundances and star-formation histories in more detail and thus obtain a deeper understanding of star formation in dwarf galaxies hosting CCSN. New, deeper all sky-surveys such as ATLAS ([Tonry et al. 2018](#)) and ZTF ([Fremling et al. 2018](#)), and eventually LSST, will increase the

sample size of host unbiased samples of CCSNe and SLSNe significantly — as will comprehensive analysis of completed surveys (e.g. iPTF; Schulze et al. in prep).

ACKNOWLEDGEMENTS

We would like to thank N. Blagorodnova and S. Kulkarni for their Keck data and S. Kim and S. Schulze for kindly allowing us to use their Magellan data for LGRB 150518A. We acknowledge useful feedback from R. Lunnan and M. Modjaz, and useful conversations with A. Wetzel and D. Bersier. DAP thanks the Aspen Center for Physics for providing a stimulating host environment during the completion of this work. The ACP is supported by National Science Foundation grant PHY-1607611. This work was partially supported by a grant from the Simons Foundation.

Some of the data presented herein were obtained at the W. M. Keck Observatory, which is operated as a scientific partnership among the California Institute of Technology, the University of California and the National Aeronautics and Space Administration. The Observatory was made possible by the generous financial support of the W. M. Keck Foundation. We recognise and acknowledge the very significant cultural role and reverence that the summit of Maunakea has always had within the indigenous Hawaiian community. We are most fortunate to have the opportunity to conduct observations from this mountain. This work is based in part on observations made with the *Spitzer Space Telescope*, which is operated by the Jet Propulsion Laboratory, California Institute of Technology under a contract with NASA. Support for this work was provided by NASA through an award issued by JPL/Caltech. This paper includes data gathered with the 6.5 meter Magellan Telescopes located at Las Campanas Observatory, Chile.

REFERENCES

- Adami C., et al., 2006, [A&A](#), **451**, 1159
- Anderson J. P., et al., 2018, [Nature Astronomy](#), **2**, 574
- Angus C. R., Levan A. J., Perley D. A., Tanvir N. R., Lyman J. D., Stanway E. R., Fruchter A. S., 2016, [MNRAS](#), **458**, 84
- Arcavi I., et al., 2010, [ApJ](#), **721**, 777
- Arcavi I., McCully C., Hosseinzadeh G., Howell D. A., Valenti S., Trakhtenbrot B., 2017, [The Astronomer's Telegram](#), **10668**
- Ashall C., et al., 2019, [MNRAS](#), **p.** 1522
- Barkat Z., Rakavy G., Sack N., 1967, [Physical Review Letters](#), **18**, 379
- Bazin G., et al., 2009, [A&A](#), **499**, 653
- Benetti S., Ochner P., Cappellaro E., Tomasella L., Turatto M., Colombo L., 2017, [The Astronomer's Telegram](#), **11072**, 1
- Benetti S., et al., 2018, [MNRAS](#), **476**, 261
- Bersier D., et al., 2006, [ApJ](#), **643**, 284
- Bianchi L., Herald J., Efremova B., Girardi L., Zabot A., Marigo P., Conti A., Shiao B., 2011, [Astrophysics and Space Science](#), **335**, 161
- Blanton M. R., Kazin E., Muna D., Weaver B. A., Price-Whelan A., 2011, [AJ](#), **142**, 31
- Bose S., et al., 2018, [ApJ](#), **862**, 107
- Brinchmann J., Charlot S., White S. D. M., Tremonti C., Kauffmann G., Heckman T., Brinkmann J., 2004, [MNRAS](#), **351**, 1151
- Bruzual G., Charlot S., 2003, [Monthly Notices of the Royal Astronomical Society](#), **344**, 1000
- Calzetti D., Armus L., Bohlin R. C., Kinney A. L., Koornneef J., Storchi-Bergmann T., 2000, [ApJ](#), **533**, 682
- Cameron E., 2011, [Publ. Astron. Soc. Australia](#), **28**, 128
- Cano Z., et al., 2017a, [A&A](#), **605**, A107
- Cano Z., Wang S.-Q., Dai Z.-G., Wu X.-F., 2017b, [Advances in Astronomy](#), **2017**, 8929054

Cantiello M., Yoon S.-C., Langer N., Livio M., 2007, *A&A*, **465**, L29

Carter B. J., Fabricant D. G., Geller M. J., Kurtz M. J., McLean B., 2001, *ApJ*, **559**, 606

Castro Cerón J. M., Michałowski M. J., Hjorth J., Malesani D., Gorosabel J., Watson D., Fynbo J. P. U., Morales Calderón M., 2010, *ApJ*, **721**, 1919

Cenko S. B., et al., 2006, *PASP*, **118**, 1396

Chabrier G., 2003, *ApJ*, **586**, L133

Chambers K. C., et al., 2016, preprint, ([arXiv:1612.05560](https://arxiv.org/abs/1612.05560))

Chatzopoulos E., Wheeler J. C., 2012, *ApJ*, **760**, 154

Chen T.-W., Smartt S. J., Yates R. M., Nicholl M., Krühler T., Schady P., Dennefeld M., Inserra C., 2017a, *MNRAS*, **470**, 3566

Chen T.-W., et al., 2017b, GRB Coordinates Network, Circular Service, No. 20380, #1 (2017), 20380

Chevalier R. A., 1977, *Annual Review of Astronomy and Astrophysics*, **15**, 175

Chevalier R. A., Irwin C. M., 2011, *ApJ*, **729**, L6

Cobb B. E., 2017, GRB Coordinates Network, 22270, 1

Corsi A., et al., 2016, *ApJ*, **830**, 42

Cutri R. M., et al. 2013, VizieR Online Data Catalog, 2328

Cutri R. M., et al. 2014, VizieR Online Data Catalog, 2328

D'Elia V., et al., 2018, *A&A*, **619**, A66

Dabringhausen J., Kroupa P., Baumgardt H., 2009, *MNRAS*, **394**, 1529

De Cia A., et al., 2018, *ApJ*, **860**, 100

Della Valle M., et al., 2006, *Nature*, **444**, 1050

Dong S., et al., 2016, *Science*, 351, 257

Dong S., et al., 2017, The Astronomer's Telegram, 1049

Drake A. J., et al., 2009, *ApJ*, **696**, 870

Drout M. R., et al., 2014, *ApJ*, **794**, 23

Erben T., et al., 2005, *Astronomische Nachrichten*, **326**, 432

Fazio G. G., et al., 2004, *ApJS*, **154**, 10

Filippenko A. V., 1997, *ARA&A*, **35**, 309

Flaugher B., 2005, *International Journal of Modern Physics A*, **20**, 3121

Fremling C., Kulkarni S. R., Taggart K., Perley D., 2018, The Astronomer's Telegram, 11615, 1

Fremling U. C., et al., 2019, arXiv e-prints, p. [arXiv:1910.12973](https://arxiv.org/abs/1910.12973)

Frieman J. A., et al., 2008, *AJ*, **135**, 338

Frohmaier C., Sullivan M., Nugent P. E., Goldstein D. A., DeRose J., 2017, *The Astrophysical Journal Supplement Series*, **230**, 4

Fruchter A. S., et al., 2006, *Nature*, **441**, 463

Furlong M., et al., 2015, *MNRAS*, **450**, 4486

Fynbo J. P. U., et al., 2006, *Nature*, **444**, 1047

Gal-Yam A., 2012, *Science*, **337**, 927

Gal-Yam A., et al., 2006, *Nature*, **444**, 1053

Galama T. J., et al., 1998, *Nature*, **395**, 670

Gehrels N., et al., 2006, *Nature*, **444**, 1044

Ginzburg S., Balberg S., 2012, *ApJ*, **757**, 178

Gorosabel J., et al., 2005, *A&A*, **444**, 711

Graur O., Bianco F. B., Huang S., Modjaz M., Shivvers I., Filippenko A. V., Li W., Eldridge J. J., 2017a, *ApJ*, **837**, 120

Graur O., Bianco F. B., Modjaz M., Shivvers I., Filippenko A. V., Li W., Smith N., 2017b, *ApJ*, **837**, 121

Gutiérrez C. P., et al., 2018, *Monthly Notices of the Royal Astronomical Society*, **479**, 3232

Hadjiyska E., et al., 2012, in New Horizons in Time Domain Astronomy. pp 324–326, doi:[10.1017/S1743921312000944](https://doi.org/10.1017/S1743921312000944)

Hjorth J., et al., 2003, *Nature*, **423**, 847

Hjorth J., et al., 2012, *ApJ*, **756**, 187

Hodgkin S. T., Wyrzykowski L., Blagorodnova N., Koposov S., 2013, *Philosophical Transactions of the Royal Society of London Series A*, **371**, 20120239

Holoiien T. W.-S., et al., 2017a, *MNRAS*, **464**, 2672

Holoiien T. W.-S., et al., 2017b, *MNRAS*, **467**, 1098

Holoiien T. W.-S., et al., 2017c, *MNRAS*, **471**, 4966

Holoiien T. W.-S., et al., 2019, *MNRAS*, **484**, 1899

Huchra J. P., et al., 2012, *ApJS*, **199**, 26

Ilbert O., et al., 2006, *A&A*, **457**, 841

Izzo L., et al., 2019, *Nature*, **565**, 324

Jarrett T. H., Chester T., Cutri R., Schneider S. E., Huchra J. P., 2003, *ApJ*, **125**, 525

Kaiser N., et al., 2002, in Survey and Other Telescope Technologies and Discoveries. pp 154–164, doi:[10.1117/12.457365](https://doi.org/10.1117/12.457365)

Kaiser N., et al., 2010, in Ground-based and Airborne Telescopes III. p. 77330E, doi:[10.1117/12.859188](https://doi.org/10.1117/12.859188)

Kasen D., Bildsten L., 2010, *ApJ*, **717**, 245

Kato D., et al., 2007, *PASJ*, **59**, 615

Keller S. C., et al., 2007, *Publications of the Astronomical Society of Australia*, **24**, 1

Kelly P. L., Kirshner R. P., 2012, *ApJ*, **759**, 107

Kelly P. L., Filippenko A. V., Fox O. D., Zheng W., Clubb K. I., 2013, *ApJ*, **775**, L5

Kennicutt Jr. R. C., 1998, *ARA&A*, **36**, 189

Komatsu E., et al., 2011, *ApJS*, **192**, 18

Krühler T., et al., 2015, *A&A*, **581**, A125

Law N. M., et al., 2009, *Publications of the Astronomical Society of the Pacific*, **121**, 1395

Lawrence A., et al., 2007, *MNRAS*, **379**, 1599

Lee J. C., Kennicutt Robert C. J., Funes S. J. J. G., Sakai S., Akiyama S., 2009, *ApJ*, **692**, 1305

Lee J. C., et al., 2011, *ApJS*, **192**, 6

Leger A., Puget J. L., 1984, *A&A*, **500**, 279

Leloudas G., et al., 2011, *A&A*, **530**, A95

Leloudas G., et al., 2015, *MNRAS*, **449**, 917

Leloudas G., et al., 2016, *Nature Astronomy*, **1**, 0034

Lilly S. J., Le Fevre O., Hammer F., Crampton D., 1996, *ApJ*, **460**, L1

Lunnan R., et al., 2014, *ApJ*, **787**, 138

Lupton R., Blanton M. R., Fekete G., Hogg D. W., O'Mullane W., Szalay A., Wherry N., 2004, *PASP*, **116**, 133

Maeder A., Meynet G., 2000, *Annual Review of Astronomy and Astrophysics*, **38**, 143

Magnier E. A., et al., 2016, preprint, ([arXiv:1612.05242](https://arxiv.org/abs/1612.05242))

Mangano V., et al., 2007, *A&A*, **470**, 105

Margutti R., et al., 2007, *A&A*, **474**, 815

Margutti R., et al., 2017, *ApJ*, **836**, 25

Martin D. C., et al., 2005, *ApJ*, **619**, L1

Mazzali P. A., et al., 2006, *ApJ*, **645**, 1323

McLean I. S., et al., 2010, in Ground-based and Airborne Instrumentation for Astronomy III. pp 77351E–77351E–12, doi:[10.1117/12.856715](https://doi.org/10.1117/12.856715)

McLean I. S., et al., 2012, in Ground-based and Airborne Instrumentation for Astronomy IV. p. 84460J, doi:[10.1117/12.924794](https://doi.org/10.1117/12.924794)

Metzger B. D., Margalit B., Kasen D., Quataert E., 2015, *MNRAS*, **454**, 3311

Michałowski M. J., et al., 2009, *ApJ*, **693**, 347

Michałowski M. J., et al., 2014, *A&A*, **562**, A70

Michałowski M. J., et al., 2015, *A&A*, **582**, A78

Mirabal N., Halpern J. P., O'Brien P. T., 2007, *ApJ*, **661**, L127

Modjaz M., Kewley L., Bloom J. S., Filippenko A. V., Perley D., Silverman J. M., 2011, *ApJ*, **731**, L4

Modjaz M., et al., 2019, arXiv e-prints, p. [arXiv:1901.00872](https://arxiv.org/abs/1901.00872)

Moriya T., Tominaga N., Tanaka M., Maeda K., Nomoto K., 2010, *ApJ*, **717**, L83

Moriya T. J., Blinnikov S. I., Tominaga N., Yoshida N., Tanaka M., Maeda K., Nomoto K., 2013, *MNRAS*, **428**, 1020

Mould J. R., et al., 2000, *ApJ*, **529**, 786

Neill J. D., et al., 2011, *ApJ*, **727**, 15

Nicholl M., et al., 2014, *MNRAS*, **444**, 2096

Niino Y., et al., 2017, *PASJ*, **69**, 27

Noeske K. G., et al., 2007, *ApJ*, **660**, L43

Norris J. P., Bonnell J. T., 2006, *ApJ*, **643**, 266

Oke J. B., Gunn J. E., 1983, *ApJ*, **266**, 713

Oke J. B., et al., 1995, *PASP*, **107**, 375

Ovaldsen J.-E., et al., 2007, *ApJ*, **662**, 294

Pastorello A., et al., 2015, *MNRAS*, **453**, 3649

Peng C. Y., Ho L. C., Impey C. D., Rix H.-W., 2002, *AJ*, **124**, 266

Perley D. A., 2019, *PASP*, **131**, 084503

Perley D. A., et al., 2009, *ApJ*, **696**, 1871

Perley D. A., et al., 2016a, *ApJ*, **817**, 7
 Perley D. A., et al., 2016b, *ApJ*, **817**, 8
 Perley D. A., et al., 2016c, *ApJ*, **830**, 13
 Persson S. E., et al., 2013, *PASP*, **125**, 654
 Podsiadlowski P., Joss P. C., Hsu J. J. L., 1992, *ApJ*, **391**, 246
 Prajs S., et al., 2017, *MNRAS*, **464**, 3568
 Prentice S., et al., 2017, The Astronomer's Telegram, **11060**, 1
 Prieto J. L., Stanek K. Z., Beacom J. F., 2008, *ApJ*, **673**, 999
 Prieto J. L., et al., 2012, *ApJ*, **745**, 70
 Prochaska J. X., et al., 2004, *ApJ*, **611**, 200
 Quimby R. M., et al., 2011, *Nature*, **474**, 487
 Quimby R. M., Yuan F., Akerlof C., Wheeler J. C., 2013, *MNRAS*, **431**, 912
 Quimby R. M., et al., 2018, *ApJ*, **855**, 2
 Rakavy G., Shaviv G., 1967, *ApJ*, **148**, 803
 Rest A., et al., 2011, *ApJ*, **729**, 88
 Sako M., et al., 2008, *AJ*, **135**, 348
 Salim S., et al., 2007, *ApJS*, **173**, 267
 Schirmer M., 2013, *ApJS*, **209**, 21
 Schlafly E. F., Finkbeiner D. P., 2011, The Astrophysical Journal, **737**, 103
 Schulze S., et al., 2014, *A&A*, **566**, A102
 Schulze S., et al., 2018, *Monthly Notices of the Royal Astronomical Society*, **473**, 1258
 Sedgwick T. M., Baldry I. K., James P. A., Kelvin L. S., 2019, *MNRAS*, **484**, 5278
 Shappee B. J., et al., 2014, *ApJ*, **788**, 48
 Smartt S. J., 2009, *Annual Review of Astronomy and Astrophysics*, **47**, 63
 Soderberg A. M., et al., 2004, *ApJ*, **606**, 994
 Soderberg A. M., et al., 2010, *Nature*, **463**, 513
 Sollerman J., et al., 2006, *A&A*, **454**, 503
 Sorokina E., Blinnikov S., Nomoto K., Quimby R., Tolstov A., 2016, *ApJ*, **829**, 17
 Stanway E. R., Levan A. J., Tanvir N., Wiersema K., van der Horst A., Mundell C. G., Guidorzi C., 2015, *MNRAS*, **446**, 3911
 Starling R. L. C., et al., 2011, *MNRAS*, **411**, 2792
 Suzuki A., Maeda K., Shigeyama T., 2019, *ApJ*, **870**, 38
 Svensson K. M., Levan A. J., Tanvir N. R., Fruchter A. S., Strolger L.-G., 2010, *MNRAS*, **405**, 57
 Thöne C. C., et al., 2008, *ApJ*, **676**, 1151
 Thöne C. C., de Ugarte Postigo A., García-Benito R., Leloudas G., Schulze S., Amorín R., 2015, *MNRAS*, **451**, L65
 Tomasella L., et al., 2016, The Astronomer's Telegram, **9610**, 1
 Tonry J. L., et al., 2018, *PASP*, **130**, 064505
 Toy V. L., et al., 2016, *ApJ*, **818**, 79
 Tremonti C. A., et al., 2004, *ApJ*, **613**, 898
 Turatto M., Benetti S., Tomasella L., Cappellaro E., Elias-Rosa N., Ochner P., Terraner G., 2016, The Astronomer's Telegram, **9829**, 1
 Vallely P. J., et al., 2018, *MNRAS*, **475**, 2344
 Volnova A., et al., 2017, GRB Coordinates Network, Circular Service, No. 20442, #1 (2017), 20442
 Vreeswijk P. M., et al., 2017, *ApJ*, **835**, 58
 Wainwright C., Berger E., Penprase B. E., 2007, *ApJ*, **657**, 367
 Wang J., et al., 2018, *ApJ*, **867**, 147
 Watson D., et al., 2011, *ApJ*, **741**, 58
 Werner M. W., et al., 2004, *ApJS*, **154**, 1
 Wilson J. C., et al., 2003, in Iye M., Moorwood A. F. M., eds, Society of Photo-Optical Instrumentation Engineers (SPIE) Conference Series Vol. 4841, Proc. SPIE. pp 451–458, doi:10.1117/12.460336
 Woosley S. E., Bloom J. S., 2006, *ARA&A*, **44**, 507
 Woosley S. E., Blinnikov S., Heger A., 2007, *Nature*, **450**, 390
 Wright E. L., et al., 2010, *AJ*, **140**, 1868
 Xhakaj E., Rojas-Bravo C., Foley M. M., Kilpatrick C. D., Pan Y.-C., Foley R. J., 2017, The Astronomer's Telegram, **10620**
 Yasuda N., et al., 2001, *AJ*, **122**, 1104
 Yoon S.-C., Langer N., Norman C., 2006, *A&A*, **460**, 199
 York D. G., et al., 2000, *AJ*, **120**, 1579
 Young D. R., et al., 2010, *A&A*, **512**, A70
 Yusof N., et al., 2013, *MNRAS*, **433**, 1114

Zhang J., Wang X., 2014, The Astronomer's Telegram, **6827**, 1
 de Ugarte Postigo A., et al., 2016, GRB Coordinates Network, Circular Service, No. 20342, #1 (2016), 20342
 de Ugarte Postigo A., Izzo L., Kann D. A., Thoene C. C., Pesev P., Scarpa R., Perez D., 2017, GRB Coordinates Network, **22204**, 1
 van den Heuvel E. P. J., Portegies Zwart S. F., 2013, *ApJ*, **779**, 114

APPENDIX A: HOST GALAXY PHOTOMETRY

In this section we present the photometry used in the spectral energy distribution fits for all the host galaxies in our sample.

APPENDIX B: PHYSICAL PROPERTIES OF HOST GALAXIES

Tables of physical properties of all host galaxies, including their stellar masses and star-formation rates. Redshifts are derived from host galaxy unless there is no redshift available.

APPENDIX C: SPECTRAL ENERGY DISTRIBUTION FITS

APPENDIX D: REFERENCES FOR PHOTOMETRY

This section contains references to all the photometry gathered from archival sources.

APPENDIX E: COMPARISONS WITH PREVIOUS WORK

We can gain further insights by examining the fraction of CCSNe exploding in dwarf galaxies. There have been a handful of studies of CCSN hosting dwarf galaxies from untargeted surveys Young et al. (2010); Prieto et al. (2012). Recently, Anderson et al. (2018) have begun a large-scale study of supernovae in dwarf galaxies to get follow-up of dwarf galaxies (fainter than -18.5 in the B -band) hosting SNe of type II, but have not specifically measured the fraction of all SNe in galaxies of this type. Arcavi et al. (2010) presented the first sample of (72) spectroscopically classified CCSN host galaxies from the Palomar Transient Factory (PTF), an untargeted (but spectroscopically incomplete) survey for supernovae. They studied the integrated properties of the hosts and found 22 per cent of CCSN supernova are in ‘dwarf’ galaxies, which they define in terms of r -band luminosity ($M_r > -18$ mag). We find a substantial fraction (40 per cent) of CCSN hosts are in galaxies with stellar masses $< 1 \times 10^9 M_\odot$, which is broadly consistent with their conclusion that a large (but non-majority) fraction of star-formation occurs in subluminous galaxies.

Spectroscopic studies of CCSN host galaxies show diversity within subclasses of the CCSN population. Specifically, recent studies suggest that highly stripped progenitor stars that explode as Ic supernovae may be found more often in higher-metallicity galaxies (Prieto et al. 2008; Leloudas et al. 2011; Modjaz et al. 2011) with higher sSFRs (Kelly & Kirshner 2012) than non-stripped envelope CCSNe. In addition, the galaxies that a sequence of decreasing metallicity has been established from from Ic -(Ib/Ib) (Modjaz et al. 2019). On the other hand, the Ic-BL subclass may prefer metal-poor galaxies (Modjaz et al. 2019). The ASAS-SN sample is dominated by Type II SNe (71) with only a small number of stripped-envelope events (8 Ibc and 4 Iib and 1 Ib/c-BL), so we are unable to address these differences.

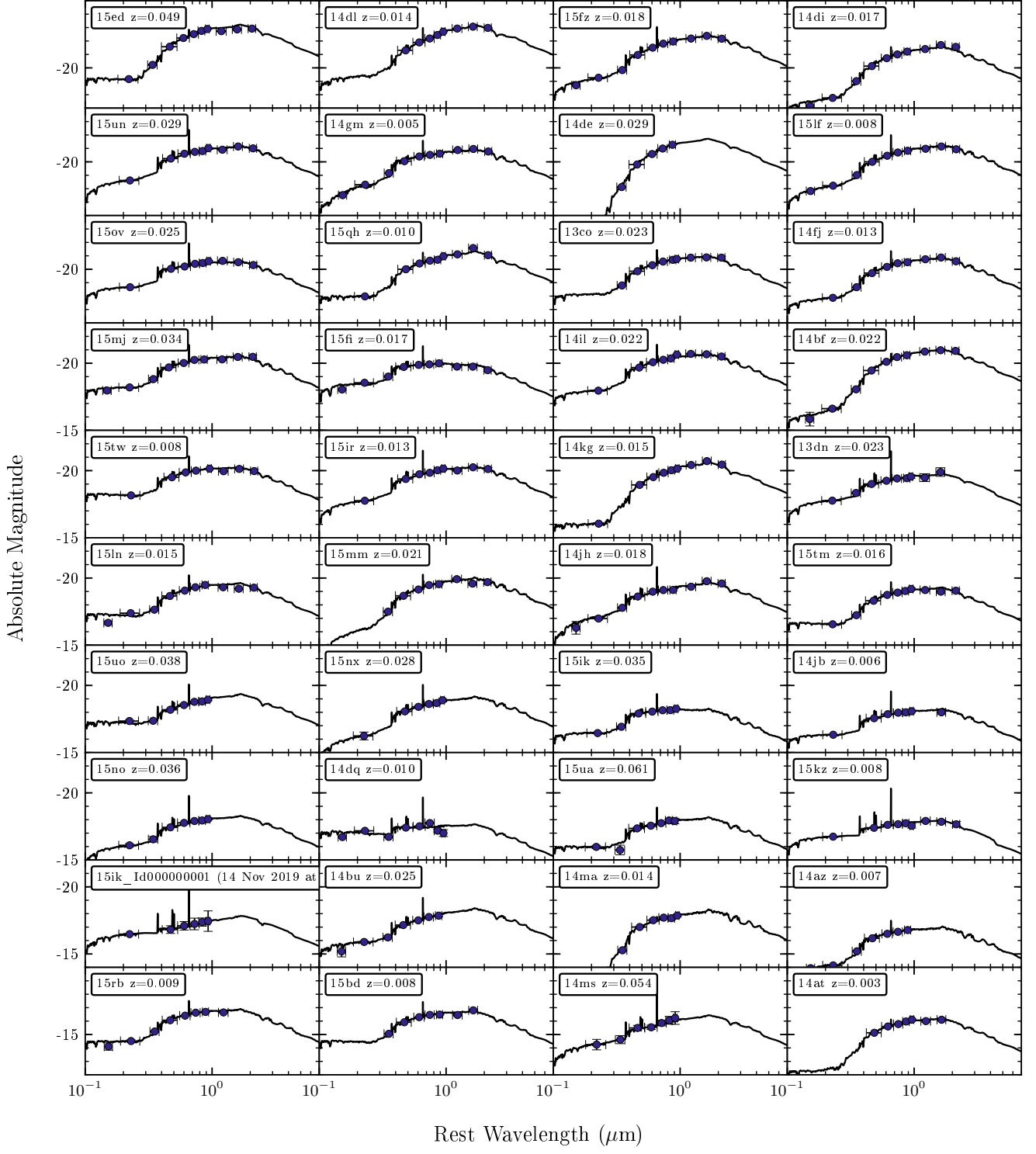
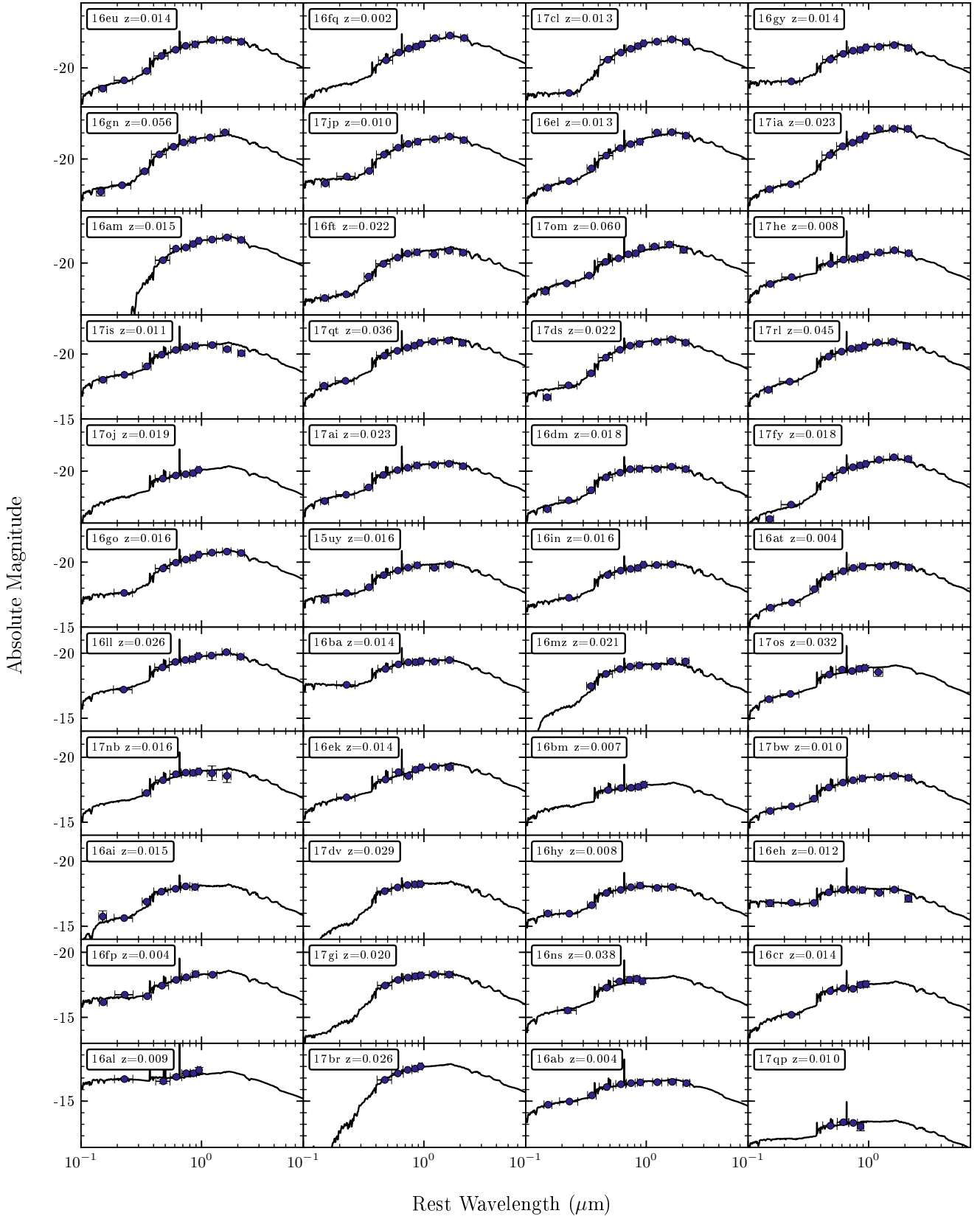


Figure C1. Spectral energy distributions of the CCSN host galaxy sample. The multi-band photometry is shown as blue markers and error bars show photometric uncertainties. The best-fit SED model is displayed by the black curve, fitted to our data using the procedure outlined in Section 4.1. Galaxies are ordered in terms of their luminosity as measured in the r -band via the SED. The absolute magnitude axis uses appropriate limits for each row.

**Figure C1 – continued**

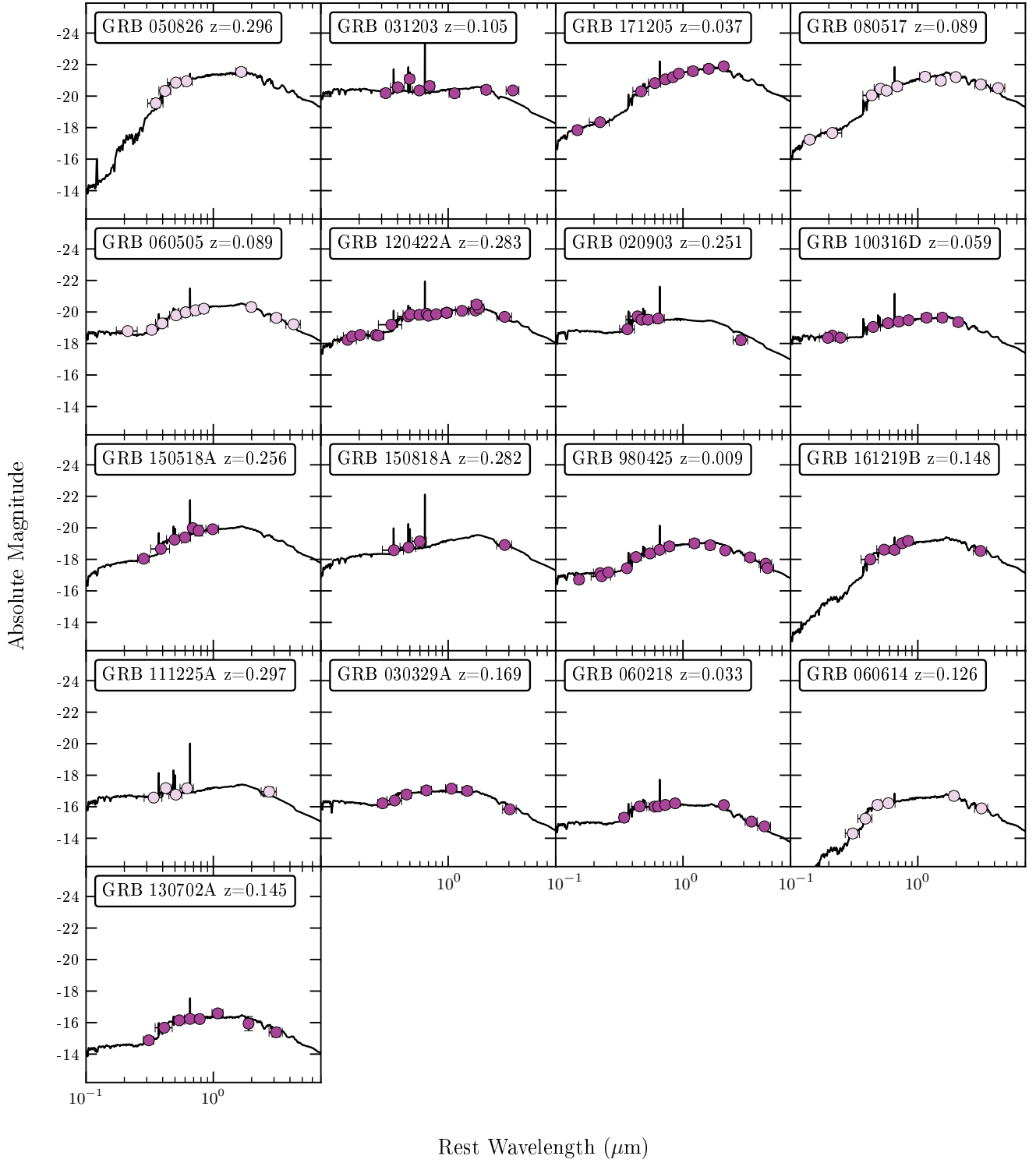


Figure C2. Spectral energy distributions of the LGRB sample. The multi-band photometry for LGRBs with SN are dark purple markers whereas LGRBs without SN are light purple and error bars show photometric uncertainties. The best-fit SED model is displayed by the black curve, fitted to our data using the procedure outlined in Section 4.1. Galaxies are ordered in terms of their luminosity as measured in the r -band via the SED. The absolute magnitude axis uses appropriate limits for each row.

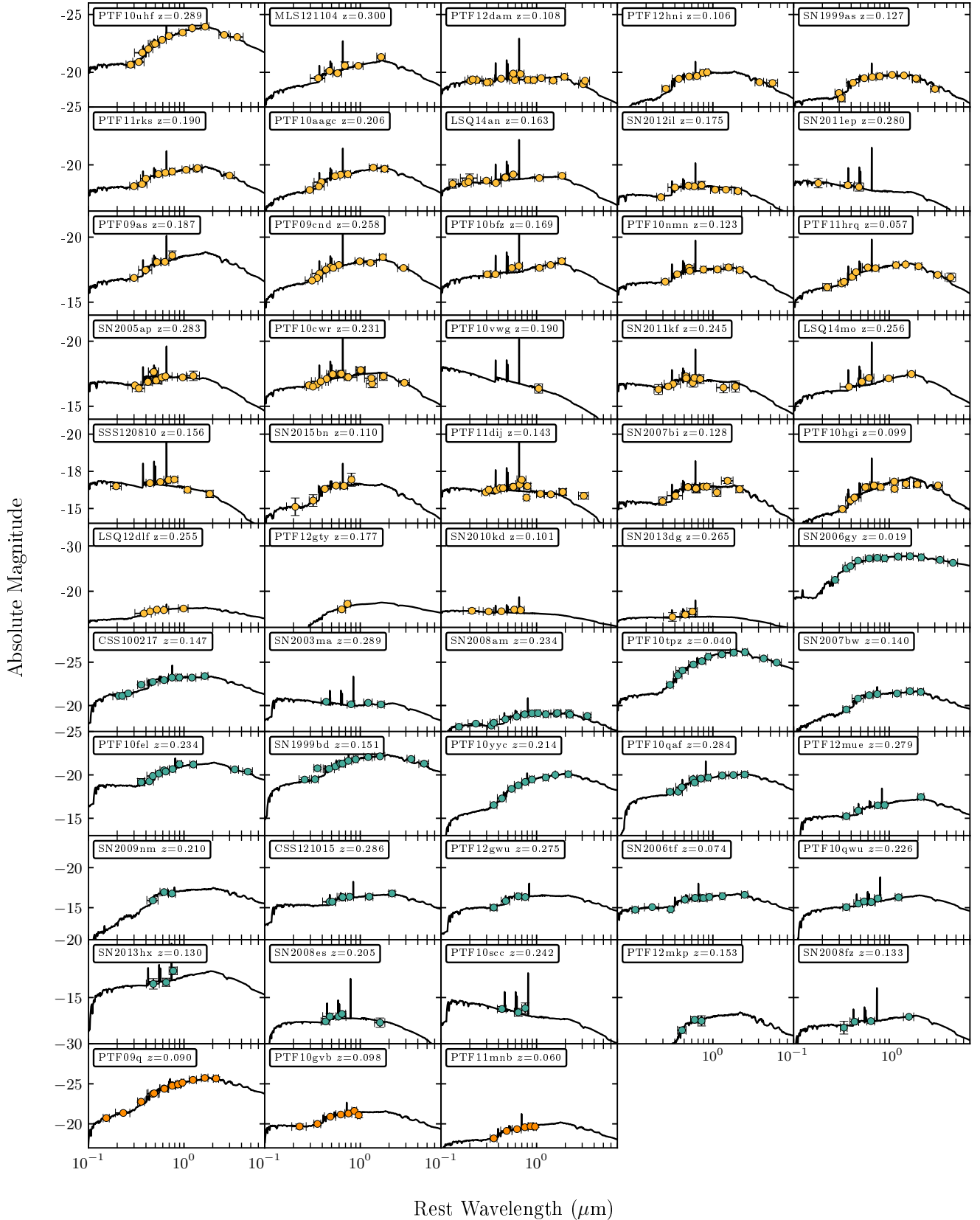


Figure C3. Spectral energy distributions of the SLSN sample. The multi-band photometry for SLSN-I are yellow markers, green for SLSN-II, and orange for possible SLSN-I and error bars show photometric uncertainties. The best-fit SED model is displayed by the black curve, fitted to our data using the procedure outlined in Section 4.1. Galaxies are ordered in terms of their luminosity as measured in the r -band via the SED. The absolute magnitude axis uses appropriate limits for each row.

Table A1. Photometry of all galaxy samples including ASAS-SN CCSN, LGRBs and SLSN used in our analysis. These data include new photometry, photometry from public data and data gathered from the literature. Only the first few lines are shown; the full table will be made available online.

Type	Name	Filter	Mag	Unc	System	Extinction	Instrument	Ref
CCSN	ASAS-SN13co	u'	16.54	0.05	std	no	SDSS	(1)
CCSN	ASAS-SN13co	g'	15.39	0.01	std	no	SDSS	(1)
CCSN	ASAS-SN13co	r'	14.88	0.01	std	no	SDSS	(1)
CCSN	ASAS-SN13co	i'	14.57	0.01	std	no	SDSS	(1)
CCSN	ASAS-SN13co	z'	14.39	0.01	std	no	SDSS	(1)
CCSN	ASAS-SN13co	y'	14.34	0.05	std	no	PS1	(4)
CCSN	ASAS-SN13co	J	13.31	0.03	std	no	2MASS	(2)
CCSN	ASAS-SN13co	H	12.79	0.07	std	no	2MASS	(2)
CCSN	ASAS-SN13co	K_s	12.34	0.11	std	no	2MASS	(2)

References: [1] Nasa Sloan Atlas; [Blanton et al. \(2011\)](#), [2] 2MASS; this work, [3] *GALEX*; [Martin et al. \(2005\)](#), [4] PS1; this work, [5] 2MASS Extended Source Catalogue; [Huchra et al. \(2012\)](#), [6] SDSS; this work [7], 2MASS Large Galaxy Atlas; [Jarrett et al. \(2003\)](#).

Notes. All photometry is available online in a machine-readable form. Magnitudes are expressed in the conventional frame, this is indicated as ‘std’ under the System column, unless given in AB form in the literature where is indicated as ‘AB’. Magnitudes are not corrected for foreground extinction and under the Extinction column as ‘no’, unless unless corrected for Galactic foreground extinction in the literature, indicated by ‘yes’.

APPENDIX F: POTENTIAL BIASES

Several biases may affect the conclusions drawn from our SN host galaxy samples. We briefly summarise these below.

F1 CCSN

Firstly there may be biases in the CCSN sample themselves in their discovery and follow-up. However, ASAS-SN is an untargeted survey, so the biases associated with targeted surveys are minimised and since the survey is shallow and their discovery numbers are relatively small, almost all ASAS-SN discoveries are followed-up spectroscopically. During 2013–2017 ASAS-SN discovered 595 SNe, of which 585 have known classifications (98 per cent were spectroscopically confirmed) on the ASAS-SN list on their website⁸. In addition, ASAS-SN discovers one quarter of its SN in catalogued host galaxies without known redshifts ([Holoien et al. 2017a](#)), indicating that ASAS-SN is less biased against finding supernovae in uncatalogued hosts than previous low-redshift SN surveys; it also finds supernova closer to the galaxy nuclei than preceding projects.

The ASAS-SN survey is effectively flux-limited, so luminous types of CCSNe will be overpopulated in our sample compared to a volume-limited survey, possibly making our sample not a true representation of the sites of (all) massive star-formation. In particular, the Type IIn subclass of SNe (which likely represents a fairly exotic, mass-loss-intense end-phase of stellar evolution itself) and IbN SNe (analogous to IIn SN but with narrow helium lines) tend to exhibit substantially higher luminosities, causing them to be overrepresented. These events only make up 8/84 and 3/84 of our sample, so even if they are over-represented somewhat they are unlikely to exert substantial impact on the properties of the sample. Luminous (ordinary) II SNe could in principle trend towards a different host population than sub-luminous II if, for some reason, the peak luminosity of a SN was a metallicity-dependent quantity. However, [Gutiérrez et al. \(2018\)](#) found no significant difference between the properties of CCSN explosions produced in faint, low-mass galaxies and those produced in bright, high-mass galaxies, so this effect is probably also not significant.

⁸ http://www.astronomy.ohio-state.edu/~assassin/sn_list.txt

F2 SLSN

Our SLSN sample is comprised of objects from a variety of surveys. About half our sample of SLSN were discovered by PTF ([Perley et al. 2016c](#); [Quimby et al. 2018](#)), a devoted transient survey during which substantial effort was placed in securing spectroscopic classifications of as many objects as possible. Even so, only a small fraction of PTF SN could be followed-up and thus there may be biases associated with this in terms of SN classification. There may also be selection biases (associated with the contrast between the transient and the host galaxy), as explained in more detail by [Frohmaier et al. \(2017\)](#). However, efforts to identify additional SLSNe in archival PTF data have produced no high-quality candidates other than those mentioned in Table 5, so it is not likely that large numbers of SNe were missed by this effort, but we cannot yet strictly rule this out.

We constructed the rest of our sample from the literature; since we focus on low-redshift objects, many of these objects were discovered by reanalysis of old data. This SLSN sample may thus potentially be quite heterogeneous. Future surveys with a stronger emphasis on an unbiased selection and follow-up will be needed to ensure this is not the case.

F3 LGRB

To avoid cosmic evolution effects, we restricted our sample of LGRBs to events closer than $z = 0.3$, even though these represent a tiny fraction (a few percent) of all LGRBs with known redshifts. However, because most observed LGRBs do not have a successful redshift measurement, it is difficult to know whether the LGRBs that are *known* to be at $z < 0.3$ are fully representative of *all* detected LGRBs at $z < 0.3$. Low- z LGRBs are often first identified to be nearby on the basis of the appearance of their host galaxies themselves: a catalogued galaxy coincident with an afterglow is a strong motivator for spectroscopic follow-up. This means that, at a fixed redshift, a LGRB host may be more likely to enter our sample if it is luminous than if it is faint. Furthermore, because of the huge pool of LGRBs occurring at higher redshifts, it is quite possible for a LGRB to be *misidentified* as a low- z burst if it happens to align with a lower-redshift galaxy. Many of these biases are mitigated by requiring a spectroscopically-confirmed supernova in association: not only does this guarantee that the redshift is correct, but the ability to conduct such a search also ensures that the LGRB could be observed readily and excludes a wider pool of events with poor ob-

Table B1. Properties of ASAS-SN CCSN host galaxies, including physical parameters derived from the SED fitting procedure.

ASAS-SN	Class	α (2000)	δ (2000)	z_{sn}	z_{host}	Distance [†] Mpc	$E(B-V)$	$\log_{10}(M_*)$ M_{\odot}	SFR $M_{\odot} \text{ yr}^{-1}$	sSFR [‡] yr^{-1}
13co	IIP	21:40:38.74	+06:30:36.87	0.023	0.0234	100.2 \pm 7.0	0.052	9.85 \pm 0.05	0.800 \pm 0.224	-9.96 \pm 0.14
13dn	II	12:52:58.20	+32:25:09.30	0.023	0.0228	105.6 \pm 7.4	0.014	9.01 \pm 0.04	1.791 \pm 0.021	-8.69 \pm 0.01
14at	II	17:55:05.43	+18:15:26.45	0.010	0.0104	52.0 \pm 3.6	0.073	8.05 \pm 0.90	0.002 \pm 0.033	-10.65 \pm 0.19
14az	IIb	23:44:48.00	-02:07:03.17	0.007	0.0067	29.3 \pm 2.1	0.028	8.00 \pm 0.01	0.012 \pm 0.002	-9.90 \pm 0.07
14bf	IIP	13:58:12.75	+17:31:53.66	0.022	0.0225	105.4 \pm 7.4	0.026	9.97 \pm 0.02	0.198 \pm 0.001	-10.70 \pm 0.01
14bu	II	11:18:41.03	+25:09:59.88	0.025	0.0255	115.9 \pm 8.1	0.014	8.59 \pm 0.12	0.141 \pm 0.126	-9.46 \pm 0.38
14de	Ic	10:40:39.33	+39:03:52.70	0.029	0.0293	130.7 \pm 9.2	0.015	10.44 \pm 0.01	0.019 \pm 0.001	-12.20 \pm 0.07
14di	II	02:01:46.39	+26:32:41.96	0.017	0.0167	69.6 \pm 4.9	0.064	10.09 \pm 0.08	0.780 \pm 0.080	-10.17 \pm 0.04
14dl	II	12:21:51.38	-24:09:54.00	0.014	0.0139	65.2 \pm 4.6	0.068	10.91 \pm 0.01	3.589 \pm 0.058	-10.30 \pm 0.04
14dq	II	21:57:59.97	+24:16:08.10	0.010	0.0104	46.9 \pm 3.3	0.062	8.01 \pm 0.07	0.344 \pm 0.291	-8.46 \pm 0.46
14fj	II	14:40:39.50	+38:37:58.55	0.013	0.0125	61.8 \pm 4.3	0.014	9.72 \pm 0.12	0.897 \pm 0.008	-9.81 \pm 0.32
14gm	II	00:59:47.83	-07:34:19.30	0.005	0.0055	23.2 \pm 1.6	0.099	9.47 \pm 0.11	0.443 \pm 0.171	-9.80 \pm 0.01
14il	IIn	00:45:32.55	-14:15:34.60	0.022	0.0220	92.3 \pm 6.5	0.020	9.62 \pm 0.06	0.622 \pm 0.231	-9.90 \pm 0.25
14jb	IIP	22:23:16.12	-28:58:30.78	0.006	0.0060	27.3 \pm 1.9	0.017	8.46 \pm 0.11	0.251 \pm 0.006	-9.11 \pm 0.01
14jh	II	08:40:44.27	+57:15:04.91	0.018	0.0175	78.4 \pm 5.5	0.055	8.92 \pm 0.05	0.807 \pm 0.161	-9.06 \pm 0.08
14kg	II	01:44:38.38	+35:48:20.45	0.014	0.0145	60.8 \pm 4.3	0.041	9.79 \pm 0.04	0.089 \pm 0.052	-10.90 \pm 0.24
14ma	IIP	23:55:09.13	+10:12:54.21	0.014	0.0137 ¹	59.3 \pm 4.7	0.091	8.57 \pm 0.04	0.001 \pm 0.001	-12.16 \pm 0.38
14ms	Ibn	13:04:08.69	+52:18:46.50	0.054	0.0540 ¹	241.0 \pm 19.3	0.010	7.58 \pm 0.32	0.030 \pm 0.015	-9.12 \pm 0.55
15bd	IIb	15:54:38.33	+16:36:38.06	0.008	0.0078	42.1 \pm 2.9	0.030	7.73 \pm 0.03	0.019 \pm 0.004	-9.56 \pm 0.07
15ed	Ibn	16:48:25.16	+50:59:30.72	0.049	0.04866 ¹	216.4 \pm 17.3	0.022	11.02 \pm 0.01	1.259 \pm 0.003	-10.90 \pm 0.01
15fi	II	16:31:48.80	+20:24:38.50	0.017	0.0172	82.1 \pm 5.8	0.050	9.12 \pm 0.17	0.341 \pm 0.121	-9.60 \pm 0.20
15fz	II	13:35:25.14	+01:24:33.00	0.017	0.0175	84.4 \pm 5.9	0.022	10.48 \pm 0.01	9.311 \pm 0.261	-9.53 \pm 0.02
15ik	IIn	11:02:04.75	+03:30:02.66	0.035	0.0346 ²	152.2 \pm 12.2	0.048	8.48 \pm 0.04	0.081 \pm 0.003	-9.60 \pm 0.01
15ir	II	10:48:30.30	-21:38:07.95	0.013	0.0127	59.2 \pm 4.2	0.056	9.14 \pm 0.26	1.469 \pm 0.545	-9.02 \pm 0.02
15kz	IIP	13:37:18.67	-28:39:23.55	0.008	0.0080	30.5 \pm 2.2	0.053	7.95 \pm 0.11	0.789 \pm 0.072	-7.98 \pm 0.04
15lf	IIn	12:06:45.56	+67:09:24.00	0.008	0.0084	41.9 \pm 2.9	0.016	9.65 \pm 0.01	2.570 \pm 0.024	-9.30 \pm 0.01
15ln	II	00:53:41.40	+18:05:29.00	0.015	0.0150	62.8 \pm 4.4	0.042	9.40 \pm 0.11	0.230 \pm 0.007	-10.04 \pm 0.03
15mj	Ib	14:02:15.64	+33:39:40.29	0.034	0.0344	155.0 \pm 10.9	0.013	9.38 \pm 0.04	0.566 \pm 0.618	-9.63 \pm 0.34
15mm	II	15:25:23.50	+29:10:24.50	0.021	0.0215	100.5 \pm 7.1	0.021	9.53 \pm 0.16	0.386 \pm 0.281	-9.96 \pm 0.09
15no	Ic	15:38:25.30	+46:54:06.60	0.043	0.03638 ¹	160.3 \pm 12.8	0.015	8.46 \pm 0.09	0.351 \pm 0.222	-8.88 \pm 0.03
15nx	II-pec	04:43:53.19	-09:42:11.22	0.026	0.02823 ¹	123.6 \pm 9.9	0.074	8.99 \pm 0.09	0.264 \pm 0.068	-9.61 \pm 0.22
15ov	II	03:30:59.15	-18:33:23.19	0.025	0.0255	106.7 \pm 7.5	0.034	9.46 \pm 0.03	1.807 \pm 0.038	-9.20 \pm 0.01
15qh	II	22:45:13.22	-22:43:39.82	0.010	0.0102	45.0 \pm 3.2	0.026	9.93 \pm 0.01	0.519 \pm 0.175	-10.29 \pm 0.88
15rb	IIn	10:08:08.24	+19:17:59.38	0.034	0.0336	149.0 \pm 10.4	0.023	8.01 \pm 0.03	0.015 \pm 0.001	-9.88 \pm 0.09
15tm	IIP	23:27:35.60	+29:24:31.17	0.016	—	69.4 \pm 21.9	0.116	9.18 \pm 0.07	0.123 \pm 0.013	-10.13 \pm 0.02
15tw	IIP	12:50:28.05	-10:50:29.15	0.008	0.0080	36.7 \pm 2.6	0.040	9.52 \pm 0.05	0.510 \pm 0.001	-9.80 \pm 0.02
15ua	IIn	13:34:54.47	+10:59:04.69	0.061	—	273.7 \pm 23.4	0.026	8.55 \pm 0.16	0.143 \pm 0.065	-9.42 \pm 0.27
15ug	II	06:45:01.68	+63:14:59.89	0.022	0.0221 ¹	96.3 \pm 7.7	0.077	7.44 \pm 0.08	0.032 \pm 0.009	-8.96 \pm 0.27
15un	II	02:40:41.38	+16:49:51.82	0.029	0.0292	121.7 \pm 8.5	0.074	9.61 \pm 0.04	3.304 \pm 0.277	-9.01 \pm 0.01
15uo	IIn-pec	01:17:00.00	-04:56:34.10	0.038	—	167.6 \pm 22.6	0.040	8.76 \pm 0.07	0.399 \pm 0.143	-9.18 \pm 0.40
15uy	IIb	14:32:15.31	+26:19:32.02	0.016	0.0160	77.5 \pm 5.5	0.017	9.35 \pm 0.10	0.762 \pm 0.113	-9.46 \pm 0.05
16ab	II	11:55:04.25	+01:43:06.77	0.004	0.0043	26.0 \pm 1.9	0.019	7.85 \pm 0.01	0.159 \pm 0.001	-8.70 \pm 0.07
16ai	IIP	14:39:44.73	+23:23:43.27	0.015	0.0149	72.8 \pm 5.1	0.028	8.12 \pm 0.01	0.007 \pm 0.006	-10.29 \pm 0.01
16al	IIP	15:00:27.47	-13:33:09.00	0.009	0.0093	44.2 \pm 3.1	0.088	7.52 \pm 0.14	0.552 \pm 0.176	-7.75 \pm 0.09
16am	II	04:45:21.28	+73:23:41.09	0.015	0.0150	66.3 \pm 4.7	0.151	10.41 \pm 0.10	0.001 \pm 0.001	-13.90 \pm 0.16
16at	II	12:55:15.50	+00:05:59.70	0.004	0.0044	26.7 \pm 1.9	0.020	9.30 \pm 0.01	0.794 \pm 0.001	-9.40 \pm 0.01
16ba	II	09:42:29.22	-16:58:26.88	0.014	0.0139	64.6 \pm 4.5	0.058	9.26 \pm 0.03	0.316 \pm 0.031	-9.72 \pm 0.03
16bm	II	11:51:56.24	-13:25:03.07	0.007	0.0068 ¹	29.3 \pm 2.3	0.038	8.07 \pm 0.19	0.320 \pm 0.113	-8.58 \pm 0.37
16cr	II	11:42:34.65	-25:54:45.22	0.014	—	60.6 \pm 21.8	0.042	8.12 \pm 0.11	0.049 \pm 0.054	-9.52 \pm 0.45
16dm	IIP	11:37:20.64	-04:54:36.84	0.018	0.0183	86.7 \pm 6.1	0.046	9.42 \pm 0.08	0.462 \pm 0.039	-9.70 \pm 0.01
16eh	II	15:40:29.23	+00:54:36.38	0.012	0.0117	58.6 \pm 4.1	0.263	8.45 \pm 0.01	0.234 \pm 0.010	-9.04 \pm 0.04
16ek	IIb	07:20:24.16	+32:51:02.58	0.014	—	60.6 \pm 21.8	0.052	8.95 \pm 0.03	0.959 \pm 0.139	-9.01 \pm 0.05
16el	II	08:56:39.08	+52:06:10.01	0.014	0.0135	61.9 \pm 4.4	0.017	10.13 \pm 0.02	2.748 \pm 0.032	-9.70 \pm 0.01
16eu	IIP	08:44:11.05	+34:42:55.80	0.014	0.0141	64.4 \pm 4.5	0.028	10.20 \pm 0.01	5.012 \pm 0.080	-9.50 \pm 0.01

Notes. SN Type, Host Galaxy, and Discovery Reference columns come from http://www.astronomy.ohio-state.edu/~assassin/sn_list.txt, except where noted.

[†] Hubble flow distances are derived from the host galaxy if available in NED and the uncertainty is derived from the velocity calculator which accounts for the Virgo Cluster, Great Attractor and Shapley Supercluster infall velocities. If a redshift is not available in NED, we search the literature for redshifts derived from a host galaxy spectrum or narrow emission lines from the SN spectrum, in these cases we adopt an 8 per cent uncertainty in the distance (since this is the maximum uncertainty derived for the NED velocity uncertainties). Finally, if the host galaxy redshift is unknown, we use the SN redshift and give the luminosity distance, with an uncertainty on the redshift of $z=0.005$.

[‡] sSFR is based on the PDF marginalised over all the other parameters in the SED fit. Thus is slightly different from the derived SFR/Mass.

¹ Host redshift was not obtained from NED, but from another source. For 14m, 14ms and 15nx the redshift was derived from narrow emission lines of the host galaxy in the SN spectrum (Zhang & Wang 2014; Vallely et al. 2018; Bose et al. 2018). For 15ed and 15no the redshift was derived from unresolved emission lines in the host galaxy spectrum (Pastorello et al. 2015; Benetti et al. 2018)

² Host redshift was derived from spectroscopy of the host galaxies in Taggart et al. (in prep).

Table B1 – *continued*

ASAS-SN	Class	α (2000)	δ (2000)	z_{sn}	z_{host}	Distance [†] Mpc	$E(B-V)$	$\log_{10}(\text{M}_*)$ M_\odot	SFR $\text{M}_\odot \text{ yr}^{-1}$	sSFR [‡] yr^{-1}
16fp	Ib/c-BL	21:59:04.14	+18:11:10.50	0.004	0.0037	18.8 ± 1.3	0.075	$8.73^{+0.01}_{-0.03}$	$0.216^{+0.004}_{-0.002}$	$-9.37^{+0.05}_{-0.04}$
16fq	IIP	11:20:19.09	+12:58:57.20	0.002	0.00243	11.5 ± 0.8	0.030	$10.56^{+0.05}_{-0.04}$	$4.887^{+0.325}_{-0.969}$	$-9.87^{+0.08}_{-0.07}$
16ft	II	23:56:13.74	-00:32:28.44	0.022	0.0222	93.6 ± 6.6	0.028	$9.79^{+0.01}_{-0.02}$	$0.294^{+0.016}_{-0.029}$	$-10.30^{+0.01}_{-0.01}$
16gn	IIn	12:06:57.59	+27:18:04.93	0.056	0.0560	246.4 ± 17.3	0.018	$10.13^{+0.03}_{-0.05}$	$1.236^{+0.845}_{-0.421}$	$-9.99^{+0.16}_{-0.22}$
16go	II	13:02:44.26	-26:56:26.81	0.016	0.0161	80.1 ± 5.6	0.070	$9.78^{+0.01}_{-0.01}$	$0.561^{+0.004}_{-0.046}$	$-10.00^{+0.01}_{-0.03}$
16gy	II	02:21:22.77	+16:33:54.56	0.014	0.0137	56.7 ± 4.0	0.129	$10.11^{+0.12}_{-0.01}$	$1.140^{+0.614}_{-0.005}$	$-10.00^{+0.05}_{-0.01}$
16hy	II	15:26:29.52	+41:44:03.32	0.008	0.0078	41.5 ± 2.9	0.022	$8.65^{+0.03}_{-0.01}$	$0.127^{+0.066}_{-0.015}$	$-9.60^{+0.18}_{-0.01}$
16in	IIn	04:59:30.07	-28:51:39.43	0.016	0.0161	68.5 ± 4.8	0.012	$9.27^{+0.04}_{-0.12}$	$0.508^{+0.097}_{-0.097}$	$-9.60^{+0.11}_{-0.05}$
16ll	II	19:00:32.43	+54:34:09.70	0.028	0.026 ¹	113.6 ± 9.1	0.054	$9.27^{+0.13}_{-0.04}$	$1.102^{+0.175}_{-0.654}$	$-9.17^{+0.04}_{-0.62}$
16mz	II	12:04:16.91	+21:48:03.30	0.021	0.0215	99.8 ± 7.0	0.020	$9.02^{+0.04}_{-0.01}$	$0.011^{+0.025}_{-0.010}$	$-10.95^{+0.63}_{-1.23}$
16ns	II	10:04:18.59	+43:25:29.13	0.038 ²	—	167.6 ± 22.8	0.011	$8.48^{+0.12}_{-0.15}$	$0.200^{+0.067}_{-0.166}$	$-9.19^{+0.23}_{-0.79}$
17ai	Ib	12:07:18.83	+16:50:26.02	0.023	0.0231	107.0 ± 7.5	0.041	$9.46^{+0.02}_{-0.13}$	$2.624^{+0.136}_{-0.857}$	$-9.01^{+0.01}_{-0.09}$
17br	IIP	15:52:00.31	+66:18:55.27	0.026	—	113.6 ± 22.2	0.024	$8.76^{+0.05}_{-0.03}$	$0.002^{+0.008}_{-0.001}$	$-11.96^{+0.96}_{-0.73}$
17bw	II	16:58:37.69	+50:29:26.50	0.01	0.01020	44.0 ± 3.1	0.019	$8.62^{+0.18}_{-0.02}$	$0.445^{+0.057}_{-0.029}$	$-8.99^{+0.06}_{-0.01}$
17cl	II	05:02:19.58	-10:21:22.78	0.013	0.0133	56.2 ± 3.9	0.078	$10.49^{+0.01}_{-0.29}$	$0.593^{+0.017}_{-0.084}$	$-10.70^{+0.01}_{-0.01}$
17ds	II	08:03:55.21	+26:31:12.73	0.022	0.0217	95.2 ± 6.7	0.038	$10.03^{+0.04}_{-0.02}$	$0.565^{+0.063}_{-0.039}$	$-10.28^{+0.08}_{-0.03}$
17dv	Ib/c	09:52:31.22	-21:57:54.59	0.029	—	127.0 ± 22.3	0.037	$8.60^{+0.04}_{-0.02}$	$0.045^{+0.043}_{-0.043}$	$-9.92^{+0.21}_{-0.12}$
17fy	IIn	09:03:32.47	-21:20:02.73	0.018	0.0182	82.7 ± 5.8	0.140	$9.59^{+0.22}_{-0.00}$	$0.766^{+0.258}_{-0.313}$	$-9.80^{+0.05}_{-0.11}$
17gi	Ibn	14:14:48.94	-29:33:37.01	0.020	—	87.0 ± 22.0	0.057	$8.73^{+0.06}_{-0.13}$	$0.107^{+0.044}_{-0.028}$	$-9.76^{+0.24}_{-0.15}$
17he	II	09:45:48.36	-14:22:05.60	0.008	0.0081	37.4 ± 2.6	0.053	$9.50^{+0.05}_{-0.05}$	$7.096^{+0.811}_{-0.727}$	$-8.65^{+0.05}_{-0.04}$
17ia	IIP	13:10:59.29	+78:24:37.16	0.023	0.0234	100.3 ± 7.1	0.033	$10.41^{+0.01}_{-0.01}$	$2.075^{+0.058}_{-0.052}$	$-10.10^{+0.01}_{-0.01}$
17is	II	02:11:06.94	+03:50:36.63	0.011	0.0105	44.9 ± 3.1	0.036	$9.46^{+0.02}_{-0.13}$	$2.965^{+0.283}_{-1.166}$	$-9.03^{+0.03}_{-0.07}$
17jp	II	02:54:02.09	+02:58:07.71	0.010	0.0102	41.9 ± 2.9	0.095	$10.40^{+0.01}_{-0.16}$	$1.135^{+0.221}_{-0.258}$	$-10.30^{+0.11}_{-0.01}$
17nb	II	07:27:37.32	+35:36:30.64	0.016	—	69.4 ± 21.9	0.048	$8.81^{+0.05}_{-0.06}$	$0.659^{+0.033}_{-0.587}$	$-9.00^{+0.06}_{-0.92}$
17oj	II	21:44:22.95	-29:54:59.30	0.016	0.01874	82.6 ± 22.0	0.040	$9.19^{+0.19}_{-0.12}$	$2.228^{+0.834}_{-0.933}$	$-8.83^{+0.23}_{-0.36}$
17om	II	03:34:11.10	-13:56:09.37	0.08	—	363.9 ± 24.0	0.042	$9.97^{+0.04}_{-0.12}$	$6.546^{+0.620}_{-1.906}$	$-9.27^{+0.10}_{-0.04}$
17os	II	04:33:05.88	-26:07:41.34	0.032	0.0323	138.4 ± 9.8	0.035	$8.74^{+0.03}_{-0.10}$	$0.778^{+0.063}_{-0.668}$	$-8.86^{+0.07}_{-0.79}$
17qp	II	20:28:49.80	-04:22:57.29	0.01 ²	—	43.3 ± 21.7	0.050	$7.02^{+0.01}_{-0.01}$	$0.005^{+0.001}_{-0.001}$	$-8.60^{+0.30}_{-0.18}$
17qt	II	02:27:36.59	-20:42:56.18	0.036	—	158.6 ± 22.5	0.023	$9.68^{+0.04}_{-0.03}$	$1.854^{+0.193}_{-0.354}$	$-9.40^{+0.05}_{-0.05}$
17rl	Ib/c	07:15:00.04	+46:22:43.79	0.045	—	199.5 ± 22.8	0.073	$9.57^{+0.02}_{-0.02}$	$1.343^{+0.140}_{-0.587}$	$-9.42^{+0.03}_{-0.28}$

Notes. SN Type, Host Galaxy, and Discovery Reference columns come from http://www.astronomy.ohio-state.edu/~assassin/sn_list.txt, except where noted.

[†] Hubble flow distances are derived from the host galaxy if available in NED and the uncertainty is derived from the velocity calculator which accounts for the Virgo Cluster, Great Attractor and Shapley Supercluster infall velocities. If a redshift is not available in NED, we search the literature for redshifts derived from a host galaxy spectrum or narrow emission lines from the SN spectrum, in these cases we adopt an 8 per cent uncertainty in the distance (since this is the maximum uncertainty derived for the NED velocity uncertainties). Finally, if the host galaxy redshift is unknown, we use the SN redshift and give the luminosity distance, with an uncertainty on the redshift of $z=0.005$.

[‡] sSFR is based on the PDF marginalised over all the other parameters in the SED fit. Thus is slightly different from the derived SFR/Mass.

¹ Host redshift was not obtained from NED, but from another source. For 16ll, the redshift was derived from narrow emission lines of the host galaxy in the SN spectrum (Tomasella et al. 2016). For 16ns, there is no available host galaxy redshift, therefore we use the best estimate SN redshift of $z=0.038$ Turatto et al. (2016). Finally for 17qp, we use the best available redshift estimate from Benetti et al. (2017) with a 50 per cent uncertainty.

² For these cases, SN redshift was not obtained from the ASAS-SN website, but from another source. For 16ns, there is no available host galaxy redshift, therefore we use the best estimate SN redshift of $z=0.038$ Turatto et al. (2016). Finally for 17qp, we use the best available redshift estimate from Benetti et al. (2017) with a 50 per cent uncertainty.

servability which were inferred to be at low redshift *only* because of a bright host galaxy.

Still, some of these SN campaigns may have been conducted only because of the initial detection and redshift measurement of a bright host galaxy in the first place, leaving the possibility of a bias in favour of luminous galaxies and against dim ones in our sample. Whether this is likely to be a significant bias can be investigated case-by-case within our sample. For about half of the events in our sample, the LGRB was either so close that the host galaxy would have been evident almost no matter how luminous or dim it was ($z < 0.1$), or the afterglow was so bright that its redshift would have been immediately evident from absorption spectroscopy regardless of its host. About half our events fall in this category. The remaining events (which may have been missed if their host was fainter or less star-forming) include 031203, 120422A, 150518A, 150818A and

perhaps 130702A (on account of its companion). However, omitting these targets would not change our conclusions.

A more delicate issue concerns the use of LGRBs without observed associated SNe, many of which specifically have observations ruling *out* the presence of a SN at or near the luminosity of SN 1998bw. As we have noted, these could in principle represent background objects in dim high- z hosts. They could also represent variants of the short LGRB phenomenon (with T90's at the extreme of the distribution or ‘extended emission’ episodes; e.g., Norris & Bonnell 2006; Perley et al. 2009), or even something else entirely. On the other hand, they could also be genuine LGRBs whose SN was missed, dim, or dust-extinguished, and/or failed entirely (Fynbo et al. 2006).

The origins of this class are probably heterogeneous: based on examination of individual no-SN events, there is reason to think almost all of the above events are at play. For example, GRB

Table B2. Photometric properties of LGRB host galaxies.

LGRB	Class	α (2000)	δ (2000)	z	$E(B-V)$	$\log_{10}(M_*)$ M_\odot	SFR $M_\odot \text{ yr}^{-1}$	ssSFR [‡] yr^{-1}
980425	SN	19:35:03.12	-52:50:44.88	0.009	0.060	8.48 ^{+0.40} _{-0.11}	0.113 ^{+0.319} _{-0.010}	-9.43 ^{+0.23} _{-0.02}
020903	SN	22:48:42.24	-20:46:09.12	0.251	0.030	8.65 ^{+0.10} _{-0.23}	1.014 ^{+0.465} _{-0.188}	-8.66 ^{+0.41} _{-0.19}
030329A	SN	10:44:49.99	+21:31:17.76	0.169	0.030	7.71 ^{+0.33} _{-0.08}	0.086 ^{+0.016} _{-0.016}	-8.79 ^{+0.15} _{-0.06}
031203	SN	08:02:29.04	-39:51:11.88	0.105	0.937	8.50 ^{+0.01} _{-0.01}	15.520 ^{+0.844} _{-0.318}	-7.30 ^{+0.02} _{-0.01}
050826	SN-less	05:51:01.58	-02:38:35.88	0.296	0.600	9.80 ^{+0.06} _{-0.11}	1.923 ^{+1.722} _{-1.764}	-9.61 ^{+0.31} _{-0.80}
060218	SN	03:21:39.67	+16:52:01.92	0.033	0.150	7.48 ^{+0.04} _{-0.08}	0.039 ^{+0.015} _{-0.011}	-8.93 ^{+0.27} _{-0.19}
060505	SN-less	22:07:03.43	-27:48:51.84	0.089	0.020	9.57 ^{+0.02} _{-0.06}	0.766 ^{+0.097} _{-0.012}	-9.69 ^{+0.08} _{-0.03}
060614	SN-less	21:23:32.11	-53:01:36.12	0.126	0.020	7.91 ^{+0.07} _{-0.04}	0.002 ^{+0.015} _{-0.002}	-10.52 ^{+0.69} _{-1.09}
080517	SN-less	06:48:58.06	+50:44:05.64	0.089	0.110	9.80 ^{+0.03} _{-0.02}	1.500 ^{+0.096} _{-0.249}	-9.62 ^{+0.03} _{-0.07}
100316D	SN	07:10:30.53	-56:15:19.80	0.059	0.120	8.94 ^{+0.03} _{-0.08}	0.762 ^{+0.254} _{-0.086}	-9.10 ^{+0.24} _{-0.06}
111225A	SN-less	00:52:37.22	+51:34:19.5	0.297	0.229	7.42 ^{+0.23} _{-0.17}	0.259 ^{+0.086} _{-0.094}	-8.00 ^{+0.31} _{-0.42}
120422A	SN	09:07:38.42	+14:01:07.68	0.283	0.030	9.04 ^{+0.03} _{-0.03}	1.219 ^{+0.233} _{-0.280}	-9.01 ^{+0.09} _{-0.06}
130702A	SN	14:29:14.78	+15:46:26.40	0.145	0.040	7.68 ^{+0.03} _{-0.17}	0.032 ^{+0.02} _{-0.017}	-9.19 ^{+0.26} _{-0.32}
150518A	SN	15:36:48.27	+16:19:47.1	0.256	0.046	9.14 ^{+0.08} _{-0.05}	1.086 ^{+0.434} _{-0.319}	-9.12 ^{+0.23} _{-0.21}
150818A	SN	15:21:25.43	+68:20:33.0	0.282	0.021	8.67 ^{+0.13} _{-0.30}	1.489 ^{+0.906} _{-0.616}	-8.49 ^{+0.51} _{-0.35}
161219B	SN	06:06:51.43	-26:47:29.52	0.148	0.028	9.03 ^{+0.07} _{-0.14}	0.228 ^{+0.176} _{-0.059}	-9.79 ^{+0.49} _{-0.16}
171205A	SN	11:09:39.52	-12:35:18.34	0.037	0.045	10.11 ^{+0.02} _{-0.08}	2.897 ^{+0.158} _{-0.261}	-9.63 ^{+0.03} _{-0.02}

Notes. [‡]sSFR is based on the PDF marginalised over all the other parameters in the SED fit. Thus is slightly different from the derived SFR/Mass.

060614's redshift is unambiguous but a very distinct host galaxy with almost no star-formation may point towards a different progenitor; GRB 051109B had no SN follow-up (despite a massive host, due to poor observability) and may simply be a missed low- z LGRB, though it could also be a background event; the SN in GRB 020903 has been interpreted as having been dust-extinguished (Soderberg et al. 2004).

Given these uncertainties, we have run our tests both including and excluding the no-SN events; our basic conclusion is unaffected by this choice, although this largely reflects the small sample size of no-SN events. Further work will be needed to securely ascertain whether the no-SN events are associated with a different progenitor.

F4 Redshift evolution

Our CCSN sample spans redshifts between $0.002 < z < 0.08$. In contrast, our SLSN and LGRB samples are predominately at redshifts greater than 0.08. While we have used a simple procedure to correct for evolution in star-formation rate, we have not made any correction for stellar mass build-up from $z = 0.3$ to 0 (as a result of galaxy mergers and from the conversion of gas into new stars) because this change is very slow across the redshift range of our sample: much less than the differences that we see or the size of our statistical errors. See Fig. 2. of (Furlong et al. 2015) who find almost no evolution in the in galaxy masses from $z = 0.3$ to 0, except for high-mass galaxies. However since the number of very high mass galaxies is small in our samples, we do not attempt to correct for this.

Changes in star-formation rate over this redshift range ($z = 0$ –0.3) are present—and while we have corrected for the offset of the main sequence, we have not corrected for possible changes in the distribution of SFR as a function of stellar mass along the main sequence. While these changes are anticipated to be small for most galaxy masses, the number of actively star-forming, very massive galaxies ($\gtrsim 10^{11} M_\odot$) strongly decreases from $z = 0.3$ to current day due to high-mass galaxy quenching. Thus, high- z transients are more likely to be found in very high-mass galaxies than low- z transients. This is not taken into account by our analysis, but the

number of very high mass galaxies is small in all samples, so its effect is likely to be minor.

F5 Extinction effect

All our SN samples are selected via an optical search and thus are subject to biases if the transient is not easily visible or identifiable due to significant obscuration by dust. This bias is common among all SN searches that discover SN at optical wavelengths. This is especially important if the transient itself is intrinsically low-luminosity or if it is discovered at high redshift (and thus selected in the rest-frame UV). Since all of our samples are exclusively at low-redshift ($z \sim 0$ –0.3), this effect should be relatively minor and it would affect all three samples in similar ways.

F6 Age effect

An additional effect we must consider is the results of difference in stellar population ages, associated with different progenitor lifetimes, between our samples. Stars that explode as SLSNe and LGRBs are likely $> 12 M_\odot$ and hence have short lifetimes of a few million years. Conversely, our sample of CCSN is dominated by type II SNe which typically originate from less massive stars of 8 – $12 M_\odot$ which may take up to a few tens of millions of years to explode. Therefore, the galaxy populations hosting CCSNe could evolve significantly more than the galaxies hosting SLSN/LGRBs after the actual star-formation episode—such that even if the properties of the galaxies were identical at the time that the SN progenitors were formed, the observable properties may in some cases be different at the time of the SN explosion.

This effect is crucial when considering precise spatial positions within the galaxy, and to some extent when dealing with emission-line metrics. Fortunately, this issue is lessened in our study because our investigations are limited to quantities derived from the broadband photometry. These wavelengths trace star-formation over a much longer timescale (10–100 Myr) than other tracers of star formation such as H α which measure the ‘instantaneous’ star-formation (1–10 Myr). Thus, the difference between

Table B3. Photometric properties of the SLSN host galaxies.

SLSN	Class	α (2000)	δ (2000)	z	$E(B-V)$	$\log_{10}(M_*)$ M_\odot	SFR $M_\odot \text{ yr}^{-1}$	sSFR [‡] yr^{-1}
LSQ12dlf	I	01:50:29.80	-21:48:45.4	0.255	0.011	7.64 ^{+0.24} _{-0.39}	0.030 ^{+0.022} _{-0.010}	-9.17 ^{+0.73} _{-0.46}
LSQ14an	I	12:53:47.83	-29:31:27.2	0.163	0.074	8.20 ^{+0.08} _{-0.19}	1.791 ^{+2.941} _{-0.358}	-7.97 ^{+0.62} _{-0.13}
LSQ14mo	I	10:22:41.53	-16:55:14.4	0.256	0.065	7.64 ^{+0.16} _{-0.23}	0.331 ^{+0.101} _{-0.213}	-8.11 ^{+0.33} _{-0.09}
MLS121104	I	02:16:42.51	+20:40:08.5	0.30	0.150	9.28 ^{+0.14} _{-0.38}	3.828 ^{+2.411} _{-1.485}	-8.70 ^{+0.61} _{-0.37}
PTF09as	I	12:59:15.864	+27:16:40.58	0.187	0.008	8.52 ^{+0.11} _{-0.23}	0.265 ^{+0.028} _{-0.029}	-9.12 ^{+0.26} _{-0.14}
PTF09cnd	I	16:12:08.839	+51:29:16.01	0.258	0.021	8.29 ^{+0.05} _{-0.04}	0.284 ^{+0.083} _{-0.101}	-8.82 ^{+0.16} _{-0.26}
PTF10aagc	I	09:39:56.923	+21:43:17.09	0.206	0.022	8.89 ^{+0.04} _{-0.08}	1.076 ^{+0.215} _{-0.297}	-8.82 ^{+0.10} _{-0.21}
PTF10bfz	I	12:54:41.288	+15:24:17.08	0.169	0.018	7.59 ^{+0.16} _{-0.06}	1.052 ^{+0.073} _{-0.526}	-7.57 ^{+0.09} _{-0.45}
PTF10cwr	I	11:25:46.73	-08:49:41.9	0.231	0.035	7.71 ^{+0.17} _{-0.09}	0.553 ^{+0.073} _{-0.395}	-7.95 ^{+0.14} _{-0.72}
PTF10hgi	I	16:37:47.074	+06:12:31.83	0.099	0.074	7.88 ^{+0.03} _{-0.04}	0.101 ^{+0.003} _{-0.006}	-8.86 ^{+0.05} _{-0.08}
PTF10nmn	I	15:50:02.809	-07:24:42.38	0.123	0.138	7.94 ^{+0.06} _{-0.11}	0.248 ^{+0.280} _{-0.066}	-8.55 ^{+0.45} _{-0.18}
PTF10uhf	I	16:52:46.696	+47:36:21.76	0.289	0.018	11.08 ^{+0.01} _{-0.06}	7.278 ^{+0.596} _{-0.941}	-10.21 ^{+0.03} _{-0.04}
PTF10vwg	I	18:59:32.881	+19:24:25.74	0.1901	0.467	7.59 ^{+0.07} _{-0.08}	0.078 ^{+0.030} _{-0.077}	-8.58 ^{+0.02} _{-0.01}
PTF11dij	I	13:50:57.798	+26:16:42.44	0.143	0.011	7.01 ^{+0.01} _{-0.01}	0.327 ^{+0.108} _{-0.009}	-7.34 ^{+0.27} _{-0.03}
PTF11hrq	I	00:51:47.22	-26:25:10.0	0.057	0.012	8.18 ^{+0.14} _{-0.06}	0.366 ^{+0.050} _{-0.210}	-8.59 ^{+0.10} _{-0.55}
PTF11rks	I	01:39:45.528	+29:55:27.43	0.19	0.038	9.02 ^{+0.03} _{-0.05}	0.741 ^{+0.128} _{-0.056}	-9.15 ^{+0.11} _{-0.05}
PTF12dam	I	14:24:46.228	+46:13:48.64	0.108	0.100	8.14 ^{+0.01} _{-0.01}	14.490 ^{+0.578} _{-0.199}	-7.00 ^{+0.01} _{-0.01}
SN1999as	I	09:16:30.86	+13:39:02.2	0.127	0.096	9.04 ^{+0.03} _{-0.03}	0.379 ^{+0.170} _{-0.202}	-9.49 ^{+0.18} _{-0.29}
SN2005ap	I	13:01:14.83	+27:43:32.3	0.283	0.026	7.73 ^{+0.05} _{-0.09}	0.129 ^{+0.020} _{-0.018}	-8.62 ^{+0.13} _{-0.11}
SN2007bi	I	13:19:20.00	+08:55:44.0	0.128	0.084	7.55 ^{+0.14} _{-0.23}	0.070 ^{+0.026} _{-0.030}	-8.72 ^{+0.36} _{-0.38}
SN2010kd	I	12:08:01.11	+49:13:31.1	0.101	0.021	7.21 ^{+0.12} _{-0.03}	0.135 ^{+0.014} _{-0.081}	-7.50 ^{+0.09} _{-1.04}
SN2011ep	I	17:03:41.78	+32:45:52.6	0.28	0.020	7.75 ^{+0.32} _{-0.29}	0.916 ^{+0.059} _{-0.649}	-7.75 ^{+0.15} _{-0.46}
SN2011kf	I	14:36:57.53	+16:30:56.6	0.245	0.069	7.52 ^{+0.11} _{-0.50}	0.144 ^{+0.649} _{-0.021}	-8.38 ^{+0.16} _{-0.15}
SN2012il	I	09:46:12.91	+19:50:28.7	0.175	0.069	8.11 ^{+0.02} _{-0.03}	0.142 ^{+0.016} _{-0.012}	-8.95 ^{+0.06} _{-0.11}
SN2013dg	I	13:18:41.38	-07:04:43.1	0.265	0.042	7.59 ^{+0.09} _{-0.02}	0.021 ^{+0.005} _{-0.001}	-8.59 ^{+0.03} _{-0.18}
SN2015bn	I	11:33:41.57	+00:43:32.2	0.11	0.022	7.75 ^{+0.21} _{-0.23}	0.076 ^{+0.018} _{-0.072}	-8.86 ^{+0.28} _{-1.37}
SSS120810	I	23:18:01.82	-56:09:25.7	0.156	0.017	7.02 ^{+0.18} _{-0.01}	0.562 ^{+0.362} _{-0.235}	-7.22 ^{+0.21} _{-0.34}
PTF09q	I [†]	12:24:50.11	+08:25:58.8	0.09	0.021	10.45 ^{+0.01} _{-0.01}	3.155 ^{+0.007} _{-0.017}	-9.90 ^{+0.01} _{-0.01}
PTF10gzb	I [†]	12:15:32.28	+40:18:09.5	0.098	0.022	8.76 ^{+0.08} _{-0.17}	0.330 ^{+0.097} _{-0.187}	-9.25 ^{+0.22} _{-0.37}
PTF11mbb	I [†]	00:34:13.25	+02:48:31.4	0.0603	0.016	8.67 ^{+0.06} _{-0.07}	0.297 ^{+0.184} _{-0.099}	-9.20 ^{+0.28} _{-0.23}
PTF12gty	I	16:01:15.23	+21:23:17.4	0.1768	0.061	8.24 ^{+0.07} _{-0.18}	0.025 ^{+0.007} _{-0.005}	-9.81 ^{+0.13} _{-0.01}
PTF12hni	I	22:31:55.86	-06:47:49.0	0.1056	0.054	9.15 ^{+0.05} _{-0.03}	0.142 ^{+0.700} _{-0.045}	-9.97 ^{+0.66} _{-0.24}
CSS100217	II	10:29:12.56	+40:42:20.0	0.147	0.013	9.84 ^{+0.03} _{-0.03}	11.510 ^{+1.825} _{-0.195}	-9.63 ^{+0.43} _{-0.35}
CSS121015	II	00:42:44.34	+13:28:26.5	0.286	0.076	7.91 ^{+0.22} _{-0.29}	0.516 ^{+0.195} _{-0.238}	-8.21 ^{+0.44} _{-0.46}
PTF10fel	II	16:27:31.103	+51:21:43.45	0.234	0.017	9.87 ^{+0.04} _{-0.06}	0.863 ^{+0.259} _{-0.259}	-9.93 ^{+0.13} _{-0.16}
PTF10qaf	II	23:35:42.887	+10:46:32.57	0.284	0.070	9.24 ^{+0.03} _{-0.12}	0.498 ^{+0.187} _{-0.022}	-9.54 ^{+0.20} _{-0.05}
PTF10qwu	II	16:51:10.572	+28:18:07.62	0.226	0.040	7.34 ^{+0.10} _{-0.15}	0.230 ^{+0.045} _{-0.072}	-7.99 ^{+0.22} _{-0.30}
PTF10scc	II	23:28:10.495	+28:38:31.10	0.242	0.093	7.16 ^{+0.01} _{-0.04}	0.018 ^{+0.002} _{-0.007}	-7.64 ^{+0.10} _{-0.19}
PTF10tpz	II	21:58:31.74	-15:33:02.6	0.040	0.041	10.68 ^{+0.10} _{-0.05}	0.458 ^{+1.316} _{-0.256}	-11.09 ^{+0.69} _{-0.40}
PTF10yyc	II	04:39:17.297	-00:20:54.5	0.214	0.041	9.77 ^{+0.04} _{-0.09}	0.230 ^{+0.178} _{-0.066}	-10.45 ^{+0.38} _{-0.12}
PTF12gwu	II	15:02:32.876	+08:03:49.47	0.275	0.033	7.81 ^{+0.19} _{-0.15}	0.106 ^{+0.018} _{-0.034}	-8.78 ^{+0.21} _{-0.44}
PTF12mkp	II	08:28:35.092	+65:10:55.60	0.153	0.046	7.36 ^{+0.16} _{-0.21}	0.005 ^{+0.003} _{-0.002}	-9.45 ^{+1.11} _{-0.43}
PTF12muc	II	03:18:51.072	-11:49:13.55	0.279	0.062	8.76 ^{+0.08} _{-0.12}	0.382 ^{+0.288} _{-0.092}	-9.17 ^{+0.39} _{-0.20}
SN1999bd	II	09:30:29.17	+16:26:07.8	0.151	0.096	9.50 ^{+0.20} _{-0.02}	1.380 ^{+0.092} _{-0.650}	-9.33 ^{+0.02} _{-0.53}
SN2003ma	II	05:31:01.88	-70:04:15.9	0.289	0.348	8.76 ^{+0.03} _{-0.06}	14.290 ^{+0.743} _{-0.293}	-7.60 ^{+0.08} _{-0.04}
SN2006gy	II	03:17:27.06	+41:24:19.5	0.019	0.493	10.76 ^{+0.14} _{-0.04}	0.001 ^{+0.001} _{-0.001}	-16.48 ^{+0.79} _{-0.73}
SN2006tf	II	12:46:15.82	+11:25:56.3	0.074	0.023	7.97 ^{+0.04} _{-0.06}	0.075 ^{+0.014} _{-0.011}	-9.11 ^{+0.12} _{-0.08}
SN2007bw	II	17:11:01.99	+24:30:36.4	0.14	0.046	9.42 ^{+0.03} _{-0.07}	1.199 ^{+2.038} _{-1.043}	-9.33 ^{+0.46} _{-0.93}
SN2008am	II	12:28:36.25	+15:35:49.1	0.234	0.078	9.38 ^{+0.04} _{-0.03}	2.761 ^{+0.667} _{-0.706}	-8.96 ^{+0.13} _{-0.15}
SN2008es	II	11:56:49.13	+54:27:25.7	0.205	0.037	7.02 ^{+0.01} _{-0.01}	0.013 ^{+0.005} _{-0.005}	-7.78 ^{+0.41} _{-0.59}
SN2008fz	II	23:16:16.60	+11:42:47.5	0.133	0.132	7.02 ^{+0.01} _{-0.01}	0.011 ^{+0.003} _{-0.008}	-8.26 ^{+0.26} _{-0.84}
SN2009nm	II	10:05:24.54	+51:16:38.7	0.21	0.011	8.63 ^{+0.42} _{-0.34}	0.200 ^{+0.107} _{-0.091}	-9.40 ^{+0.67} _{-0.60}
SN2013hx	II	01:35:32.83	-57:57:50.6	0.13	0.022	7.49 ^{+0.20} _{-0.14}	0.019 ^{+0.008} _{-0.012}	-8.66 ^{+0.53} _{-0.99}

Notes. [†] Possible SLSN-I are indicated

[‡]sSFR is based on the PDF marginalised over all the other parameters in the SED fit. Thus is slightly different from the derived SFR/Mass.

SLSN and CCSN is not likely to be an age effect. If a galaxy is starting from a very small stellar population and then a starburst begins, many more young stars will have formed in the tens of millions of years between the explosions of the first very high-mass stars and the explosions of stars with longer lifetimes. Thus, there may be a mass ‘build-up’ effect seen in CCSNe opposed to SLSNe and

LGRBs, leading to systematically higher masses. However, this effect is only important for the very youngest, lowest-mass galaxies, of which we have demonstrated that there are very few.

Table D1. LGRB photometry sources. The cases where LGRBs do have SNe, but there is no known SN name designation on TNS we use SN in the name column.

LGRB	SN name	Reference
980425	1998bw	[2,3,4]
020903	SN	[1,5,6]
030329A	2003dh	[1,7]
031203	2003lw	[1,8,9,10]
050826	–	[1,11,12]
060218	2006aj	[1,13,14]
060505	–	[4,14,15,16]
060614	–	[1,14,17,18]
080517	–	[1,19]
100316D	2010bh	[20,21]
111225A	–	[1,22]
120422A	2012bz	[1,23]
130702A	2013dx	[1,24]
150518A	SN	[1]
150818A	SN	[1]
161219B	2016jca	[1,25]
171205	2017iuk	[1,26,27]

References:

[1] This work, [2] Michałowski et al. (2009), [3] Michałowski et al. (2014), [4] Castro Cerón et al. (2010), [5] Bersier et al. (2006), [6] Wainwright et al. (2007), [7] Gorosabel et al. (2005), [8] Margutti et al. (2007), [9] Mazzali et al. (2006), [10] Prochaska et al. (2004), [11] Ovaldsen et al. (2007), [12] Mirabal et al. (2007), [13] Sollerman et al. (2006), [14] Hjorth et al. (2012), [15] Thöne et al. (2008), [16] Wright et al. (2010), [17] Mangano et al. (2007), [18] Gal-Yam et al. (2006), [19] Stanway et al. (2015), [20] Starling et al. (2011), [21] Michałowski et al. (2015), [22] Niino et al. (2017), [23] Schulze et al. (2014), [24] Toy et al. (2016), [25] Cano et al. (2017b), [26] Bianchi et al. (2011), [27] Huchra et al. (2012).

Notes. New photometry measurements for the LGRBs are detailed in Section 3.5 and is included in online machine-readable table.

F7 Differences in Photometry Procedure

We use broad-band photometry and SED fitting using LE PHARE to derive stellar masses and SFRs of each galaxy sample. Thus, the samples are well homogenised since the same modelling technique is used on all samples. The photometry from PTF SLSN and CCSN are done using a similar method. There may, however, be differences in background and aperture treatment for photometry measurements we have taken from the literature—but in most cases this photometry is directly validated by comparison to our own measurements, with measurements that disagree to high significance excluded.

In addition, the dominant source of uncertainty for the photometry of nearby and massive galaxies in the CCSN sample is from the background subtraction. Therefore the photometric uncertainties may be underestimated for these sources. However, we gather some photometry from the NSA which has a special background optimised subtraction and these host galaxies are not offset from the rest of the sample.

This paper has been typeset from a \TeX / \LaTeX file prepared by the author.

Table D2. SLSN archival photometry sources

SLSN	TNS Name	Type	Reference
LSQ12dlf	—	I	[1,2]
LSQ14an	—	I	[1,3]
LSQ14mo	—	I	[1]
MLS121104	—	I	[1,4]
PTF09as	SN2009cb	I	[5]
PTF09cnd	—	I	[5,6]
PTF10aagc	—	I	[5]
PTF10bfz	—	I	[5]
PTF10cwr	SN2010gx	I	[1,4,5,6]
PTF10hgi	SN2010md	I	[1,4,5,6]
PTF10nnm	—	I	[5]
PTF10uhf	—	I	[5,7]
PTF10vwg	SN2010hy	I	[5]
PTF11dij	SN2011ke	I	[1,5,6]
PTF11hrq	—	I	[5,7]
PTF11rks	SN2011kg	I	[1,5]
PTF12dam	—	I	[1,5,7]
SN1999as	—	I	[1,5,6,7]
SN2005ap	—	I	[1,4,6,8]
SN2007bi	—	I	[1,6]
SN2010kd	—	I	[1,3]
SN2011ep	—	I	[1,3]
SN2011kf	—	I	[1,4,6]
SN2012il	—	I	[1,4,6]
SN2013dg	—	I	[1]
SN2015bn	—	I	[1,3]
SSS120810	—	I	[1]
CSS100217	—	II	[1]
CSS121015	—	II	[1]
PTF10fel	—	II	[5,7]
PTF10qaf	—	II	[5]
PTF10qwu	—	II	[5]
PTF10scc	—	II	[5]
PTF10tpz	—	II	[5,9]
PTF10yye	—	II	[5]
PTF12gwu	—	II	[5]
PTF12mkp	—	II	[5]
PTF12mue	—	II	[5]
SN1999bd	—	II	[1,6,7,10]
SN2003ma	—	II	[11,12]
SN2006gy	—	II	[6,7]
SN2006tf	—	II	[1,3]
SN2007bw	—	II	[1]
SN2008am	—	II	[1,3,6,9,13]
SN2008es	—	II	[1,6]
SN2008fz	—	II	[6]
SN2009nm	—	II	[1]
SN2013hx	—	II	[1]

References: [1] Schulze et al. (2018), [2] Nicholl et al. (2014), [3] Bianchi et al. (2011), [4] Lunnan et al. (2014), [5] Perley et al. (2016c), [6] Angus et al. (2016), [7] Cutri & et al. (2013), [8] Adami et al. (2006), [9] Cutri & et al. (2014), [10] Neill et al. (2011), [11] Kato et al. (2007), [12] Rest et al. (2011), [13] Lawrence et al. (2007), [14] Blanton et al. (2011), [15] Huchra et al. (2012).